Journal of Medicinal Chemistry

pubs.acs.org/jmc

Article

Small-Molecule Thioesters as SARS-CoV-2 Main Protease Inhibitors: Enzyme Inhibition, Structure–Activity Relationships, Antiviral Activity, and X-ray Structure Determination

Thanigaimalai Pillaiyar,*,○ Philipp Flury,○ Nadine Krüger,○ Haixia Su,○ Laura Schäkel,○ Elany Barbosa Da Silva, Olga Eppler, Thales Kronenberger, Tianqing Nie, Stephanie Luedtke, Cheila Rocha, Katharina Sylvester, Marvin R.I. Petry, James H. McKerrow, Antti Poso, Stefan Pöhlmann, Michael Gütschow, Anthony J. O'Donoghue, Yechun Xu,* Christa E. Müller, and Stefan A. Laufer

Cite This: https://doi.org/10.1021/acs.jmedchem.2c00636

Read Online

ACCESS | Metrics & More | Article Recommendations | Supporting Information

ABSTRACT: The main protease (M^{pro}, $3CL^{pro}$) of SARS-CoV-2 is an attractive target in coronaviruses because of its crucial involvement in viral replication and transcription. Here, we report on the design, synthesis, and structure–activity relationships of novel small-molecule thioesters as SARS-CoV-2 M^{pro} inhibitors. Compounds **3w** and **3x** exhibited excellent SARS-CoV-2 M^{pro} inhibition with k_{inac}/K_i of 58,700 M^{-1} s^{-1} (K_i = 0.0141 μM) and 27,200 M^{-1} s^{-1} (K_i = 0.0332 μM), respectively. In Calu-3 and Vero76 cells, compounds **3h**, **3i**, **3l**, **3r**, **3v**, **3w**, and **3x** displayed antiviral activity in the nanomolar range without host cell toxicity. Co-crystallization of **3w** and **3af** with SARS-CoV-2 M^{pro} was accomplished, and the X-ray structures showed covalent binding with the catalytic Cys145 residue of the protease. The potent SARS-CoV-2 Mpro inhibitors also inhibited the M^{pro} of other beta-coronaviruses, including SARS-CoV-1 and MERS-CoV, indicating that they might be useful to treat a broader range of coronaviral infections.

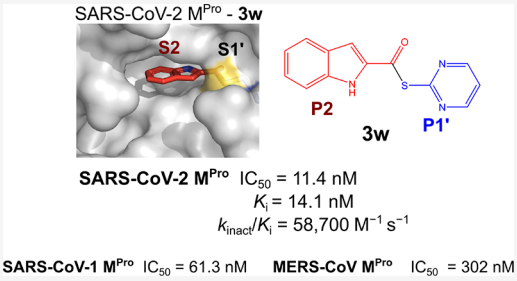

■ INTRODUCTION

The etiological agent of the current human coronavirus disease 2019 (COVID-19) is the severe acute respiratory syndrome coronavirus 2 (SARS-CoV-2). It is a global health concern due to its ability to rapidly transmit from person to person and evade human immune surveillance.[1−4] As of 25 February 2022, SARS-CoV-2 has infected around 430 million individuals globally, resulting in approximately 6 million deaths.[5] The severe disease generally occurs in the elderly or those with pre-existing medical conditions. There are more than 20 different SARS-CoV-2 vaccines in use, all of which have been shown to be effective. However, because vaccine hesitancy persists globally and breakthrough infections are prevalent in vaccinated people, efficient antiviral therapeutics are required. Furthermore, SARS-CoV-2 is constantly evolving, and vaccination effectiveness will continue to diminish as mutations accumulate.[6,7] Because of their faster transmission capacity and higher mortality,[8,9] the B.1.617.2 (Delta) and B.1.1.529 (Omicron) variants have emerged as prominent in the current pandemic.[8−10] According to new findings, available COVID-19 immunizations are less effective against the Delta and Omicron variants, and persons who have been vaccinated are still at risk of infection.[11,12]

The only direct-acting antivirals approved for emergency use are remdesivir and nirmatrelvir.[13−15] Remdesivir is an RNA-dependent RNA polymerase (RdRp) inhibitor that is given intravenously to individuals with COVID-19 infection.[13,14] Nirmatrelvir is a peptidomimetic M^{pro} inhibitor commercialized under the brand name Paxlovid in combination with ritonavir.[15]

SARS-CoV-2 is one of many beta-coronaviruses in the Coronaviridae family, also including SARS-CoV-1 and Middle East respiratory syndrome coronavirus (MERS-CoV) that were responsible for the SARS and MERS epidemics in 2003 and 2012, respectively.[16−18]

The RNA genome sequence of the SARS-CoV-2 virus offers an ideal starting point for drug discovery and the development of efficient COVID-19 treatments.[19,20] Coronaviruses are enveloped, single-stranded, nonsegmented positive-sense RNA viruses featuring the largest viral RNA genomes known to date. The genome of SARS-CoV-2 encodes two large polyproteins: pp1a (~450 kDa) and pp1ab (~750 kDa). These are extensively processed by two viral proteases, the papain-like protease (PL^{pro}) and the main protease (M^{pro}, also called $3CL^{pro}$), producing 16 nonstructural proteins (NSPs),

Received: April 22, 2022

ACS Publications © XXXX American Chemical Society

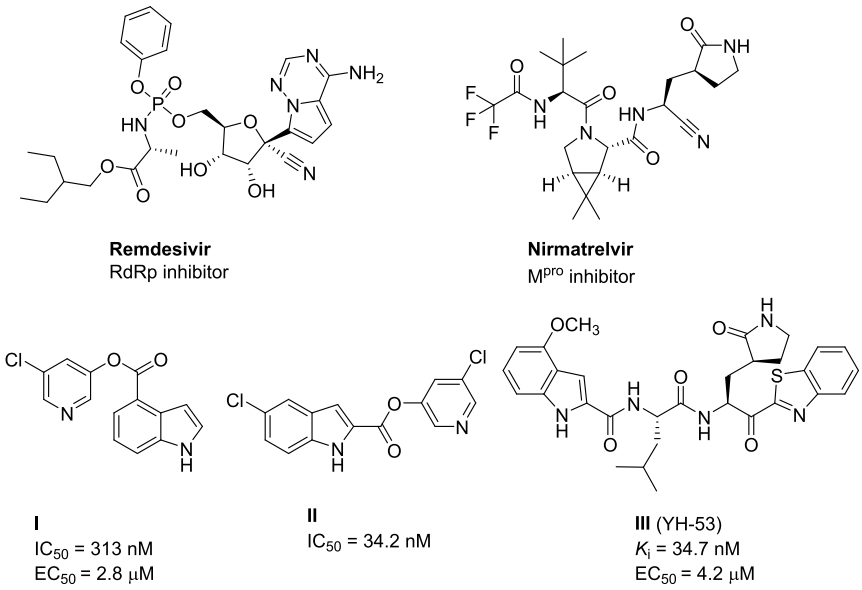

Figure 1. Structures of SARS-CoV-2 RdRp and M^{pro} inhibitors.

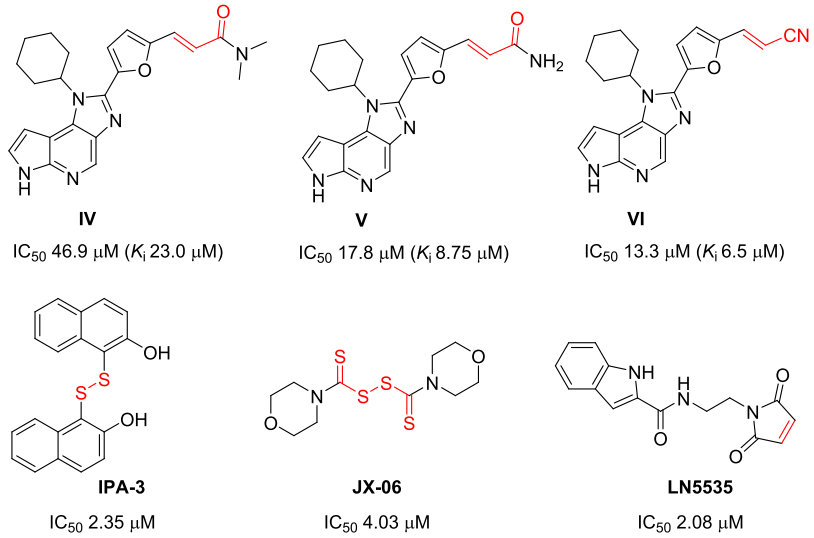

Figure 2. SARS-CoV-2 M^{pro} inhibitory activity (IC_{50}) of hit compounds identified by high-throughput screening. The proposed warhead or reactive group of the inhibitors is highlighted in red.

including the RNA-dependent RNA polymerase (RdRp), that are involved in viral replication and transcription.[21,22]

Due to the indispensable role of M^{pro} in viral replication and its high conservation among related pathogenic coronaviruses such as MERS-CoV and SARS-CoV-1, it represents a promising target for the development of broad-spectrum antiviral therapy.[16,17,23,24] Moreover, M^{pro} is unique in recognizing the substrate specificity and cleaves at the glutamine position. Because human proteases lack this property, it may be possible to develop selective protease inhibitors that are not toxic to humans. Only one human protease, kallikrein-3, has a comparable substrate specificity as M^{pro} for cleavage on the C-terminal side of glutamine. Because kallikrein-3 is a serine protease expressed solely in the prostate gland,[25] inhibitors affecting the cysteine protease M^{pro} are unlikely to target it, and if they do, inhibition will be restricted to the prostate gland.

So far, a variety of SARS-CoV-2 M^{pro} inhibitors have been reported that can be classified into covalently and noncovalently acting agents.[26−31] The active-site M^{pro} contains a catalytic dyad where Cys145 functions as a nucleophile and His41 serves as a catalytic general base. Covalent inhibitors, including small molecules and peptidomimetics, bear different warhead groups and act through a reaction with the active-site cysteine, producing a covalent bond with the inhibitor.[32−36] In continuous efforts to develop SARS-CoV-1 and SARS-CoV-2 therapeutics, we and others have developed a wide variety of substrate-derived peptidomimetic and nonpeptidic small-molecule inhibitors targeting the main protease.[23,24,28−38] In particular, a series of novel chloropyridyl ester derivatives (**I** and **II**, see Figure 1) displayed potent SARS-CoV-2 M^{pro} inhibitory activities.[37,39] The positions of an ester moiety and other substituents on the indole ring affected SARS-CoV-2 M^{pro} inhibitory potency and antiviral activity.[37,39] The indole carboxylate scaffold is thought to be important for binding to the M^{pro} active site. The unique benzothiazolyl ketone derivative (**III**, see Figure 1), which was first reported as a SARS-CoV-1 M^{pro} inhibitor,[24] also has a significant antiviral and SARS-CoV-2 M^{pro} activity.[38]

https://doi.org/10.1021/acs.jmedchem.2c00636
J. Med. Chem. XXXX, XXX, XXX−XXX

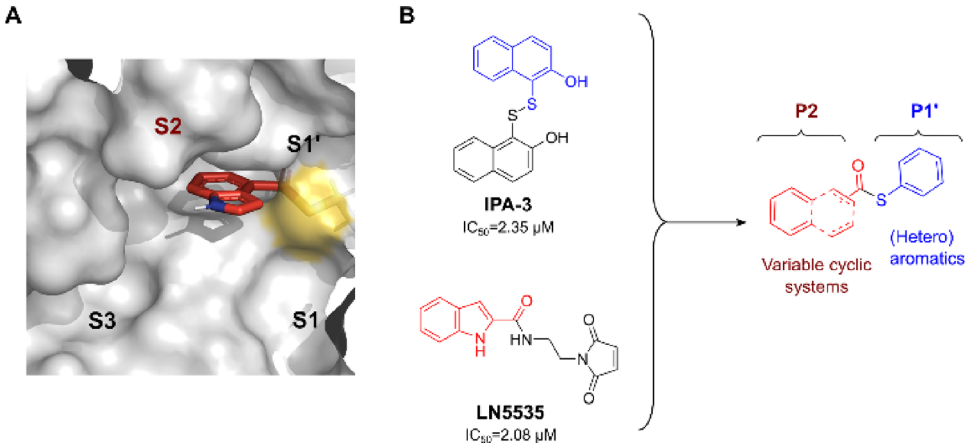

Figure 3. (A) M^{pro} active site (PDB ID: 7RC0) showing the catalytic Cys145 (yellow) and the subsites S1′, S1, S2, and S3. (B) Design of new thioesters by combining IPA-3 and LN5535.

In the present study, a virtual screening of the Tübingen Kinase Inhibitor Collection (TüKIC), containing >10,000 proprietary kinase inhibitors, was performed. Based on the results from this screen, we report the design and synthesis of a novel class of thioesters and discuss their structure−activity relationships. The compounds were tested for inhibition at recombinant SARS-CoV-2 M^{pro} employing a recently developed robust assay,[37] and enzyme inhibition kinetics were measured to elucidate the compounds' mechanism of inhibition. For potent inhibitors, antiviral activity was determined. Moreover, the co-crystallization of selected compounds with SARS-CoV-2 M^{pro} was performed to obtain insights into their molecular interactions with the target. The SARS-CoV-2 M^{pro} inhibitors were additionally tested against M^{pro} from other pathogenic beta-coronaviruses, namely, SARS-CoV-1 and MERS-CoV, which they also inhibited with high potency.

RESULTS AND DISCUSSION

Virtual Screening. The 3D structure of SARS-CoV-2 M^{pro} in association with multiple inhibitors is accessible for in silico screening to discover novel lead structures. We virtually screened our in-house TüKIC library against M^{pro}. This collection contains over 10,000 compounds that target a nucleophilic cysteine residue in a variety of kinases. Starting from the M^{pro} 3D structure,[40] we employed a pipeline combining docking with short molecular dynamics (MD) simulations of 200 ns to yield 15 selected hit molecules, which were subsequently tested for their SARS-CoV-2 M^{pro} inhibitory activity (Supporting information, Table S1).

All compounds were initially screened at 10 μM against SARS-CoV-2 M^{pro}, and three compounds, inhibiting M^{pro} by 50% or more, were chosen to determine concentration-dependent inhibition. Inhibitors **IV** and **V** showed moderate potency against M^{pro}, while **VI** had a K_i value of 6.5 μM (Figure 2). Its proposed binding mode suggests that the imidazo[4,5-*d*]pyrrolo[2,3-*b*]pyridine unit occupies the S2 pocket, displaying a stable Π−Π interaction with His41. The structure-dependent activity analysis of these three inhibitors suggests that the acrylonitrile warhead was slightly preferred for M^{pro} inhibition. Additionally, these inhibitors are selective JAK-3 inhibitors with very high potencies.[41] The inhibition of JAK-3 is a promising approach for the treatment of COVID-19 as it reduces the inflammatory/cytokine storm that is one of the major factors for the organ damage that leads to death.[42] Indeed, many JAK inhibitors are already in advanced clinical trials for the treatment of COVID-19.[43] Therefore, inhibitors targeting the viral main protease and JAK would not only have direct antiviral effects but also beneficially suppress the overproduction of cytokines induced by viral infection.

Some disulfides including IPA-3 and JX-06 were identified as hit molecules with IC_{50} values of 2.35 and 4.03 μM (Figure 2). IPA-3 was reported as a non-ATP competitive, allosteric, and reversible covalent inhibitor of dysregulated p21-activated kinase 1 (Pak1),[44] which has been linked to oncogenesis. In previous studies by us and others, disulfiram was reported as a SARS-CoV-2 M^{pro} inhibitor with IC_{50} values ranging from 7 to 9 μM.[37,45] JX-06, a morpholine derivative, was discovered as a hit molecule with a lower IC_{50} value than disulfiram. JX-06 was the first covalent 3-phosphoinositide-dependent protein kinase-1 (PDK1) inhibitor forming a reversible mixed disulfide with a conserved cysteine residue of the target.[46] We also discovered that a maleimide derivative of indole-2-carboxamide (LN5535) inhibited M^{pro} with an IC_{50} of 2.08 μM.

The active site of M^{pro} is divided into four subsites (S1′, S1, S2, and S3), each of which accommodates four fragments (P1′, P1, P2, and P3) of peptidomimetic inhibitors.[23,24] However, particularly for irreversible small-molecule inhibitors, the efficacy is frequently determined by the strength of the warhead group even when the four sites are not fully occupied.[23,24] The co-crystal structure of M^{pro} in a complex with an indole chloropyridyl ester derivative showed the acylation of the active site Cys145 to form a thioester intermediate with the indole moiety oriented toward the S2 pocket (Figure 3a).[39]

To design a novel class of inhibitors, we docked our two screening hits, IPA-3 and LN5535, at the Mpro active site (PDB ID: 7RC0) and observed that they share a similar orientation to the indole chloropyridyl ester derivative. Subsequently, we designed a novel class of thioesters by inserting variable cyclic systems from IPA-3 and the (hetero)aryl thiols from LN5535, as shown in Figure 3B. Subsequently, we designed a novel class of thioesters by inserting variable cyclic systems from IPA-3 and the (hetero)aryl thiols from LN5535, as shown in Figure 3B. We proposed that the designed new inhibitors may have a similar binding mode to that of the indole chloropyridyl ester derivatives.[39] A series of (hetero)aromatic thioesters were developed with different thiolate residues to be accommodated in the S1′ pocket. The electronic properties of (hetero)aromatic P1′ moieties may alter the reactivity of the thioester toward

https://doi.org/10.1021/acs.jmedchem.2c00636
J. Med. Chem. XXXX, XXX, XXX−XXX

Scheme 1. Synthesis of Thioesters 3a-v[a]

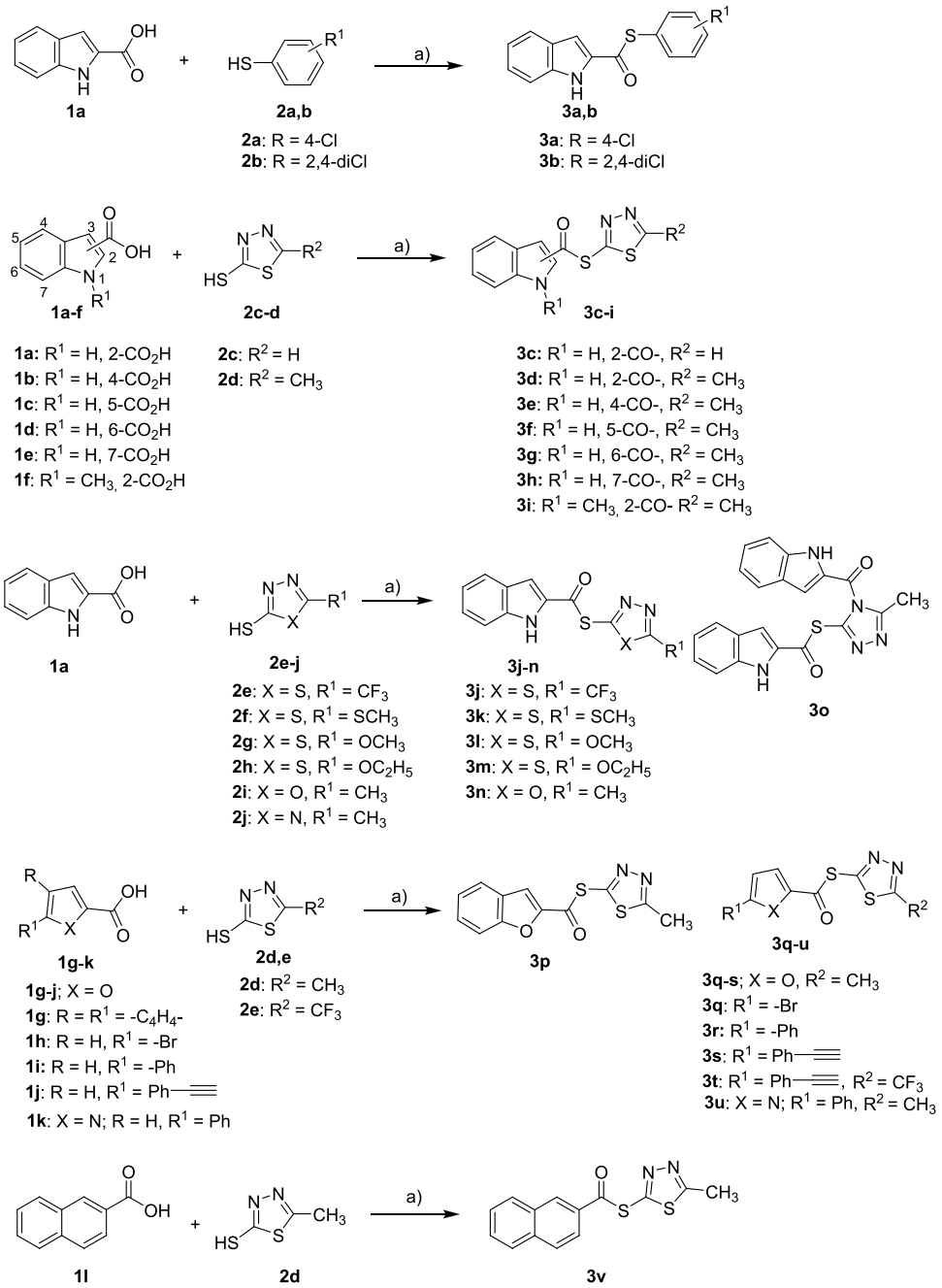

[a]Reagents and conditions: (a) $POCl_3$, pyridine, DCM, 12 h, 55−82%.

Cys145. As P2 fragments, a broad range of mono-cyclic or bi-cyclic rings with various physiochemical characteristics was investigated. This resulted in 40 novel thioesters that were evaluated against SARS-CoV-2 M^{pro}.

Chemistry. Our priority was to find the best P2 scaffold (Scheme 1). We expected indole to be optimal for inhibiting M^{pro} based on previous reports.[37,39] Several indole carboxylic acids, **1a−f**, were first treated with $POCl_3$ in dichloromethane (DCM) in the presence of pyridine, and the in situ generated carboxylic acid chlorides were subsequently reacted with thiophenols (**2a−b**) or 1,3,4-thiadiazole-2-thiol derivatives (**2c−d**) to yield compounds **3a−i** in good yields (47−80%). Compounds **3j−n** (53−73%) were obtained from differently substituted 1,3,4-thiadiazolyl-2-thiols (**2e−h**) or 5-methyl-1,3,4-oxadiazolyl-2-thiol (**2i**). The reaction of 5-methyl-4*H*-1,2,4-triazolyl-3-thiol (**2j**) with **1a** produced *S*,*N*-diacylated product **3o** in 45% yield. Simultaneously, we explored the role of the indole unit by replacing it with a variety of furan, pyrrole, and naphthalene substructures. The relevant carboxylic acids **1g−l** were reacted with the thiols **2d** or **2e**, producing a series of final products, **3p−v**, in yields ranging from 58 to 82%.

Next, the combination of P2 and P1′ moieties was investigated (Scheme 2). The P2 indole was kept constant, as in our previous strategy. The thioesters **3w−z** were obtained (48−84%) by reacting **1a** or **1l** with three pyrimidine-2-thiols (**2k−m**) under the same reaction conditions. Alternatively, pyrimidine-2-thiols were maintained and combined with various carboxylic acids (**1i−r**) to produce the products **3aa−ag**, most

https://doi.org/10.1021/acs.jmedchem.2c00636
J. Med. Chem. XXXX, XXX, XXX−XXX

Scheme 2. Synthesis of Thioesters 3w−z and 3aa−an[a]

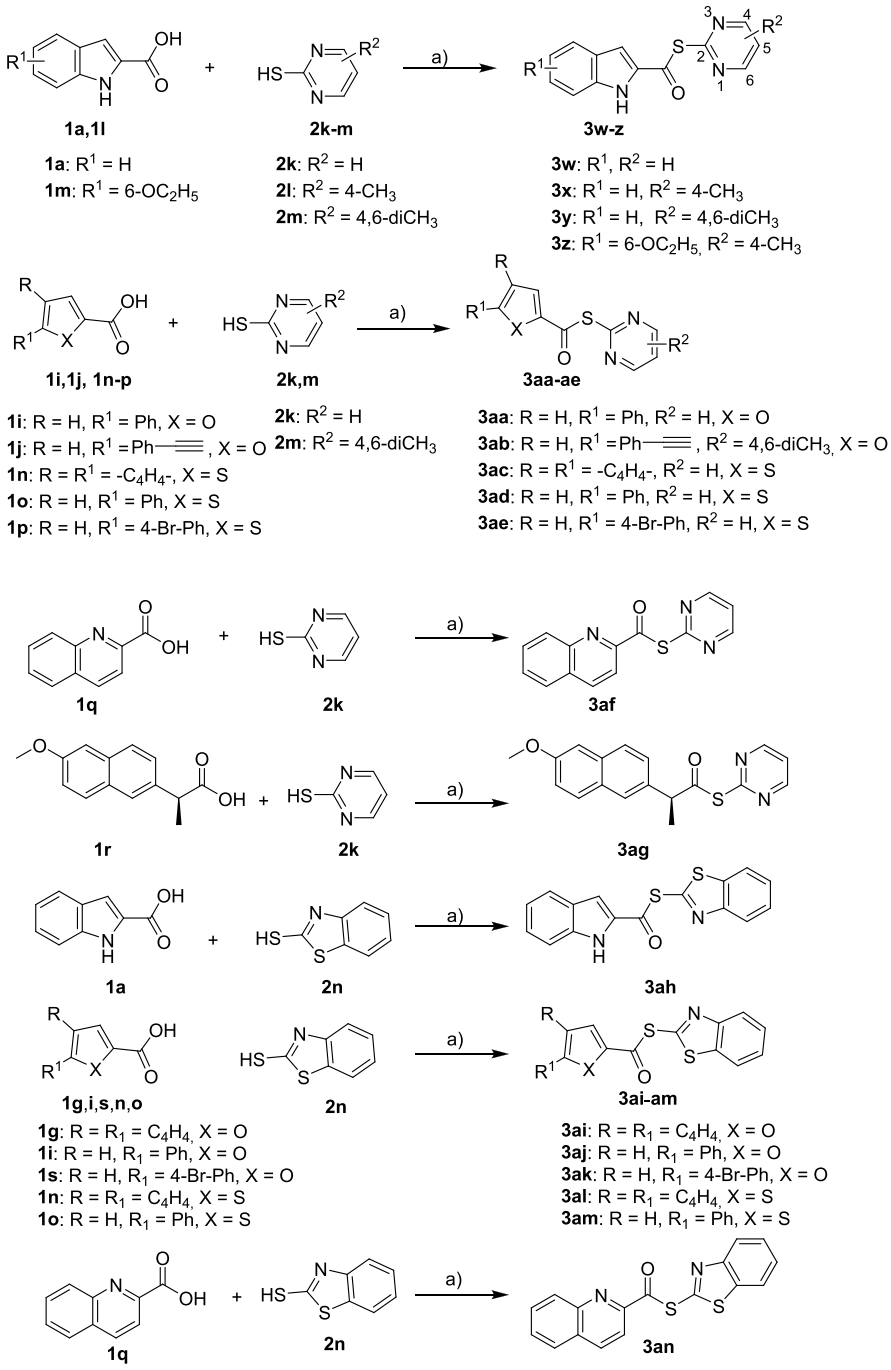

[a]Reagents and conditions: (a) $POCl_3$, pyridine, DCM, 12 h, 48−84%.

of which contained building block **2k**. The reaction of several bicyclic carboxylic acids (**1a**, **1g**, **1i**, **1s**, **1n**, **1o**, and **1q**) with the bicyclic benzo[*d*]thiazolyl-2-thiol (**2n**) yielded the final compounds **3ah**−**3an** in good yields of 56−80%.

SARS-CoV-2 M^{pro} Inhibition Assay. SARS-CoV-2 M^{pro} was expressed and purified as previously described.[37] SARS-CoV-2 M^{pro} activity assays were performed using a recently developed fluorogenic substrate (Boc-Abu-Tle-Leu-Gln-AMC),[38] and compounds were initially screened at a high concentration of 10 μM. For compounds showing M^{pro} inhibition by at least 50%, full concentration−inhibition curves were determined with at least eight different inhibitor concentrations, and the respective product formation rates were observed during the first 10 min of the enzymatic reaction. IC_{50} values were calculated by nonlinear regression analysis. For inhibitors that showed a time-dependent inhibition, the second-order rate constant k_{inac}/K_i was determined by monitoring the effects of five different inhibitor concentrations on the product formation rate for 60 min (see Table 1).

Structure−Activity Relationships. The indole-2-thioesters with 4-chlorobenzene (**3a**) and 2,4-dichlorobenzene (**3b**) did not show any inhibition of SARS-CoV-2 M^{pro}. Surprisingly, replacing the aryl ring with a heteroaromatic ring system such as 1,3,4-thiadiazole in **3c** (IC_{50} 0.143 μM) resulted in potent

https://doi.org/10.1021/acs.jmedchem.2c00636
J. Med. Chem. XXXX, XXX, XXX−XXX

Table 1. Structures and Activities of Thioesters as SARS-CoV-2 M^{pro} Inhibitors

no.	structure	SARS-CoV-2 main protease		
		IC_{50} or % inhibition at 10 μM [b]	K_i (μM) [b]	k_{inac}/K_i ($M^{-1}s^{-1}$) [a]
3a	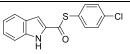	4%		
3b	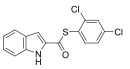	9%		
3c	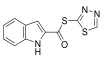	0.143 ± 0.021	0.0744	10700[b]
3d	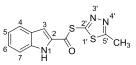	0.624 ± 0.082	n.d. [c]	n.d. [d]
3e	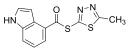	0.0600 ± 0.0257	n.d.	n.d. [d]
3f	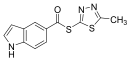	0.0723 ± 0.0221	0.393	3370
3g	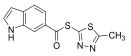	0.0547 ± 0.0073	0.186	5850
3h	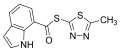	0.159 ± 0.038	0.250	3960 [b]
3i	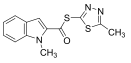	0.349 ± 0.123	0.295	7170 [b]
3j	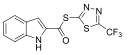	26%		
3k	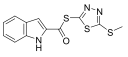	0.0914 ± 0.0163	0.0430	11800 [b]
3l	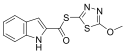	0.147 ± 0.044	0.0844	7970 [b]
3m	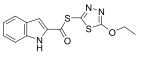	37%		
3n	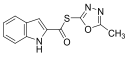	1.22 ± 0.05	0.119	3880 [b]
3o	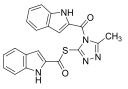	0.281 ± 0.025	0.0773	12200 [b]
3p	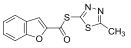	0.316 ± 0.021	0.0357	5190 [b]
3q	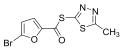	0.481 ± 0.082	n.d.	n.d. [e]
3r	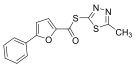	0.0344 ± 0.0072		n.d. [d]
3s	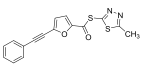	0.250 ± 0.076	0.0344	5200 [b]
3t	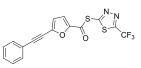	14%		

no.	structure	SARS-CoV-2 main protease		
		IC_{50} or % inhibition at 10 μM [b]	K_i (μM) [b]	k_{inac}/K_i ($M^{-1}s^{-1}$) [a]
3u	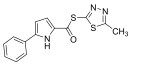	0.235 ± 0.058	0.605	5070 [b]
3v	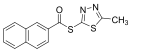	0.454 ± 0.011	0.0211	6960 [b]
3w	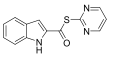	0.0114 ± 0.0028	0.0141	58700 [b]
3x	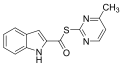	0.0876 ± 0.0109	0.0332	27200 [b]
3y	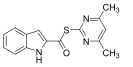	2.03 ± 0.23	0.773	1790 [b]
3z	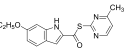	-8%		
3aa	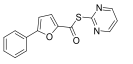	0.0181 ± 0.0039	n.d.	n.d. [d]
3ab	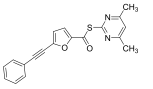	0.288 ± 0.045		n.d. [d]
3ac	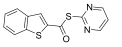	0.0155 ± 0.0045		n.d. [d]
3ad	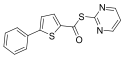	0.0137 ± 0.0039		n.d. [d]
3ae	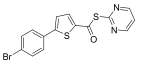	0.0144 ± 0.0020	n.d.	n.d. [d]
3af	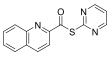	0.0206 ± 0.0006	n.d.	n.d. [d]
3ag	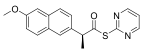	0.551 ± 0.092	0.021	33900 [a]
3ah	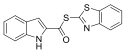	0.117 ± 0.048	0.0726	14200 [b]
3ai	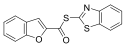	14%		
3aj	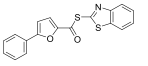	0.166± 0.027	0.612	515 [b]
3ak	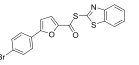	0.255± 0.048	0.013	1490 [b]
3al	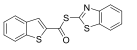	0.190± 0.039	0.161	2000 [b]
3am	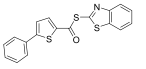	0.125± 0.039	0.042	2100 [b]
3an	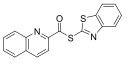	0.0889± 0.027	0.051	5450 [b]

https://doi.org/10.1021/acs.jmedchem.2c00636
J. Med. Chem. XXXX, XXX, XXX−XXX

Table 1. continued

[a]Inhibitors showed time-dependent inhibition. Progress curves in the presence of five different inhibitor concentrations were followed over 60 minutes and analyzed by nonlinear regression using the equation $[P] = v_i \times (1 - \exp(-k_{obs} \times t)/k_{obs} + d)$, where $[P]$ is the product concentration, v_i is the initial rate, k_{obs} is the observed first-order rate constant, and d is the offset. [b]The second-order rate constant, k_{inac}/K_i, was determined by plotting k_{obs} versus $[I]$ and nonlinear regression using the equation $k_{obs} = (k_{inac} \times [I])/([I] + K_i \times (1 + [S]/K_m))$. The deviation of each data point from the calculated nonlinear regression was less than 10%. [c]n.d.: not determined. [d]Compounds displayed time-dependent inhibition, but progress curves bent upward, which indicated that the inhibitor was covalently bound to the enzyme and was slowly released, hence restoring the enzyme activity. Consequently, the inhibitor concentration decreased over time due to protease-catalyzed cleavage. Such compounds were only characterized by their IC_{50} values. [e]Evaluation was not possible as progress curves were linear. The compound might have inhibited the enzyme noncovalently as k_{obs} did not increase with increasing inhibitor concentration.

inhibitory activity against M^{pro}. This inhibitor was kinetically characterized as an irreversible SARS-CoV-2 M^{pro} inhibitor, and the second-order rate constant of inactivation, k_{inac}/K_i, was 10,700 M^{-1} s^{-1} (K_i = 0.0744 μM) (**3c**, see Figure S1).

5-Methyl substitution of the 1,3,4-thiadiazole ring slightly reduced the inhibitor potency (**3d**, IC_{50} 0.624 μM). A positioning scan of the 1,3,4-thiadiazole thioester residue connected to the indole core was performed to study the chemical space of the indole thioesters. When compared to inhibitor **3d**, which bears the thioester moiety at position 2 of the indole residue, all of the regioisomeric thioesters (**3e−h**) displayed an increased inhibitory activity against M^{pro}, with the thioester moiety at position 6 being the most potent of all isomeric inhibitors (**3g**, IC_{50} 0.0547 μM). The k_{inac}/K_i for inhibitors **3d** and **3e** were not calculated due to considerable M^{pro} reactivation within 1 h; for **3f** (K_i = 0.393 μM), **3g** (K_i = 0.186 μM), and **3h** (K_i = 0.250 μM), they are 3369, 5850, and 3960 M^{-1} s^{-1}, respectively. Methylation of the indole nitrogen resulted in a 2-fold increase in inhibitory activity (**3i**, IC_{50} 0.349 μM) compared to **3d**, along with a k_{inac}/K_i value of 7170 M^{-1} s^{-1} (K_i = 0.295 μM), demonstrating that the free NH is not necessary (Table 1).

Next, the 5-methyl group on the 1,3,4-thiadiazole was exchanged for different moieties such as 5-CF_3, 5-SCH_3, 5-OCH_3, and 5-OC_2H_5 using **3d** as a lead inhibitor. The incorporation of 5-SMe (**3k**, IC_{50} 0.0914 μM) and 5-OCH_3 (**3l**) improved the potency of **3d** by up to 6-fold, whereas the 5-CF_3 (**3j**) and 5-OC_2H_5 (**3m**) replacements were disadvantageous. Inhibitors **3k** (K_i = 0.0430 μM) and **3l** (K_i = 0.0844 μM) have k_{inac}/K_i values of 11,800 (**3k**, see Figure S2) and 7970 M^{-1} s^{-1}, respectively.

The replacement of 5-methyl-1,3,4-thiadiazole with 5-methyl-1,3,4-oxadiazole reduced the inhibitory activity slightly, resulting in compound **3n** (IC_{50} 1.22 μM), which, however, displayed a sustained inhibition reaching a k_{inac}/K_i value of 3880 M^{-1} s^{-1} (K_i = 0.0773 μM). Surprisingly, the 5-methyl-4*H*-1,2,4-triazole-derived double acylated compound **3o** had higher inhibitory potency than **3d**, suggesting that there is room in the active site of the M^{pro} for the additional indole-3-carbonyl residue. **3o** has a k_{inac}/K_i value of 12,200 M^{-1} s^{-1} (K_i = 0.0773 μM) (see Figure S3).

The bioisosteric substitution of the indole moiety in **3d** by a benzofuran ring resulted in a more potent inhibitor, **3p**, with a k_{inac}/K_i value of 5190 M^{-1} s^{-1} (K_i = 0.0357 μM). Next, we continued modifying the benzofuran ring of **3p**. For example, the replacement of benzofuran by 5-bromofuran marginally reduced the affinity (**3q**), whereas 5-phenylfuran (**3r**, IC_{50} 0.0344 μM) and 5-(phenylethynyl)furan derivatives (**3s**, IC_{50} 0.250 μM) showed stronger inhibitory activity than **3p**; in particular, compound **3r** had a 14-fold higher potency. The k_{inac}/K_i values were not determined for **3q** and **3r**, but for **3s**, it was found to be 5200 M^{-1} s^{-1} (K_i = 0.0344 μM). The inhibitory activity of the trifluoromethyl analog of **3t** dropped, demonstrating once again that a 5-CF_3-1,3,4-thiadiazole thioester was not beneficial for M^{pro} inhibition. The furan ring in **3r** was exchanged for pyrrole, resulting in the inhibitor **3u**, which had a lower potency but still showed inhibitory activity in the low micromolar range. The k_{inac}/K_i value for **3u** is 5070 M^{-1} s^{-1} (K_i = 0.605 μM). Potency was somewhat increased by replacing the indole ring in **3d** by a naphthalene ring system. The resulting inhibitor, **3v**, had an IC_{50} value of 0.454 μM. The k_{inac}/K_i value for **3v** is 6960 M^{-1} s^{-1} (K_i = 0.0211 μM).

In the next attempt, we addressed the ring size of the thiolate portion. The replacement of 1,3,4-thiadiazole in **3d** with pyrimidine led to the most potent inhibitor, **3w**, of the present study. It has an IC_{50} value of 0.0114 μM and a k_{inac}/K_i value of 58,700 M^{-1} s^{-1} (K_i = 0.0141 μM) (**3w**, see Figure S4), making it a suitable scaffold for further development. The introduction of one methyl group into the 4-position of the pyrimidine ring marginally reduced inhibitory activity (**3x**, IC_{50} 0.0876 μM (k_{inac}/K_i = 27,200 M^{-1} s^{-1}, K_i = 0.0332 μM), see Figure S5), while 4,6-dimethyl substitution decreased it significantly (**3y**, IC_{50} 2.03 μM). These findings imply that the thioester with an unsubstituted pyrimidine is the best leaving group for covalent M^{pro} inhibition of the present series.

With these new warheads, we explored another part of the molecules. Initially, we incorporated a 6-ethoxy group into the indole, resulting in **3z** that had no inhibitory activity. When indole was exchanged for 5-phenylfuran resulting in inhibitor **3aa**, M^{pro} inhibition was equipotent to that of **3w** with an IC_{50} value of 0.0181 μM, but noticeable M^{pro} reactivation within 1 h was observed. Compound **3ab**, in which 5-(phenylethynyl)furan was combined with a 6-dimethylpyrimidine thioester group, displayed stronger M^{pro} inhibitory activity (IC_{50} of 0.288 μM) than **3y**; however, k_{inac}/K_i could not be calculated.

The replacement of indole by benzothiophene (**3ac**, IC_{50} 0.0155 μM), 5-phenylthiophene (**3ad**, IC_{50} 0.0137 μM), or 5-(4-*Br*-phenyl)thiophene (**3ae**, IC_{50} 0.0144 μM) resulted in outstanding M^{pro} inhibitory potency comparable to that of indole derivative **3w**, but k_{inac}/K_i values could not be calculated owing to M^{pro} reactivation. The quinolone system (**3af**) likewise demonstrated efficacy, with an IC_{50} value of 0.0206 μM. Surprisingly, the pyrimidine thioester of naproxen, a nonsteroidal anti-inflammatory drug, inhibited M^{pro} with an IC_{50} of 0.551 μM and a k_{inac}/K_i value of 33,900 M^{-1} s^{-1} (K_i = 0.021 μM) (**3ag**, K_i = 0.021 μM, see Figure S6).

Finally, we installed a benzothiazole (in **3ah**, K_i = 0.0726 μM, see Figure S7) in place of a pyrimidine (in **3w**), achieving an IC_{50} of 0.117 μM along with a high k_{inac}/K_i value of 14,200 M^{-1} s^{-1} (K_i = 0.0726 μM) (**3ah**, see Figure S7), indicating that this bicyclic thioester is also well suitable. Following this discovery, the M^{pro} inhibitory activity of a number of bicyclic benzothiazole thioesters was studied. Inhibition was lost when indole was replaced with benzofuran. However, the introduction of 5-

https://doi.org/10.1021/acs.jmedchem.2c00636
J. Med. Chem. XXXX, XXX, XXX−XXX

phenylfuran (**3aj**, IC_{50} 0.166 μM), 5-(4-*Br*-phenyl)furan (**3ak**, IC_{50} 0.255 μM), benzothiophene (**3al**, IC_{50} 0.190 μM), 5-phenylthiophene (**3am**, IC_{50} 0.125 μM), or quinoline (**3an**, IC_{50} 0.089 μM) resulted in a similar inhibitory activity as compound **3ah**, although none of these modified compounds outperformed **3ah**. The concentration−inhibition curves for selected compounds are shown in Figure 4.

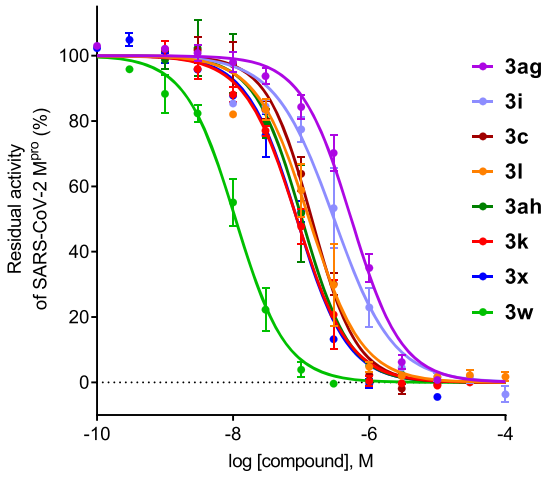

Figure 4. Concentration-dependent inhibition of SARS-CoV-2 M^{pro} by the best inhibitors of the present series: **3ag** (IC_{50} 0.551 ± 0.092 μM), **3i** (IC_{50} 0.349 ± 0.123 μM), **3c** (IC_{50} 0.143 ± 0.021 μM), **3l** (IC_{50} 0.147 ± 0.044 μM), **3ah** (IC_{50} 0.117 ± 0.048 μM), **3k** (IC_{50} 0.0914 ± 0.0163 μM), **3x** (IC_{50} 0.0876 ± 0.0109 μM), and **3w** (IC_{50} 0.0114 ± 0.0028 μM).

Cytotoxicity and Antiviral Activity against SARS-CoV-2. *Cytotoxicity.* Selected M^{pro} inhibitors were further investigated for their antiviral activity in Calu-3 and Vero 76 cells. It is worth mentioning that the cytotoxicity of test compounds reduces cell virion production, which is commonly misunderstood as antiviral activity. Therefore, we first carefully checked the cytotoxicity of M^{pro} inhibitors in both cell lines at a high concentration of 10 μM. As outlined in Figure S8, none of the tested compounds exerted cytotoxicity.

Antiviral Activity. Based on the promising inhibitory activity of the thioesters against SARS-CoV-2 M^{pro}, we evaluated the antiviral efficacy of selected potent inhibitors against SARS-CoV-2 in vitro. Calu-3 and Vero 76 cells were infected with SARS-CoV-2 to evaluate each of these M^{pro} inhibitors. The Calu-3 cell line, which is derived from human lung, is the most extensively used cellular model for assessing antiviral efficacy against respiratory pathogens in vitro. Whereas in Calu-3 cells, SARS-CoV-2 enters the cells in a TMPRSS2-dependent manner, Vero cells barely express TMPRSS2 and viral entry is mediated by cathepsins.[47]

Cells were incubated with 10 μM of each inhibitor 1 h prior to infection and 24 h post-infection (p.i.) at a multiplicity of infection (MOI) of 0.01. Viral titers of Calu-3 and Vero 76 cell culture supernatants were evaluated by titration on Vero E6 cells 24 h p.i. and are given as plaque-forming units (PFU) per milliliter (see Figure S9). As positive controls, we used remdesivir and **I**, an established SARS-M^{pro} inhibitor.[37,39]

In Figures S10 and S11, the viral titers of SARS-CoV-2 derived from Calu-3 or Vero 76 cells incubated with 10-fold serial dilutions (10−0.001 μM) of each inhibitor or DMSO (solvent control) 1 h prior and 24 h post infection (p.i.) are shown. Based on these results, dose-dependent inhibition curves were generated for all active inhibitors that exhibited EC_{50} values ranging from 0.0383 to 4.05 μM in Calu-3 (Figure 5, see Figure S12 for compounds **3f**, **3g**, **3aa**, **3ae**, and **3af**) and 0.00458 to 0.642 μM in Vero 76 cells (Figure 6), respectively.

In Calu-3 cells, the compounds **3v** (EC_{50} 0.0450 μM) and **3l** (EC_{50} 0.0383 μM) showed excellent antiviral activity (Figure 5). Compounds **3w**, **3ah**, and **3r** showed antiviral activity in the submicromolar range (0.100−0.137 μM). The pyrimidine derivative **3w**, one of the most potent M^{pro} inhibitors in the enzymatic assay, had an EC_{50} of 0.110 μM, which is around 10 times less potent than its M^{pro} inhibitory activity. The analogous benzothiazole derivative **3ah** had similar M^{pro} inhibitory (IC_{50} 0.117 μM) and antiviral activities (EC_{50} of 0.137 μM). With an EC_{50} of 0.100 μM, **3r** showed very good antiviral activity. The antiviral activities of **3c**, **3i**, **3x**, **3h**, and **3e** were also submicromolar, with EC_{50} values ranging from 0.367 to 0.734 μM. The antiviral activities of compounds **3f**, **3g**, **3aa**, **3ae**, and **3af** were lower, in the micromolar range, with EC_{50} values of 1.21−4.05 μM. In our testing system, control compounds like remdesivir and **I** possessed EC_{50} values of 0.0796 and 0.0285 μM, respectively.

In Vero 76 cells, compounds **3c**, **3i**, and **3x** were confirmed to act as anti-SARS-CoV-2 agents (see Figure S11). With an EC_{50} value of 0.00458 μM, **3i** was the most potent compound identified in this study. The antiviral activity of **3c** was maintained in Vero 76 cells with an EC_{50} of 0.641 μM, whereas the activity of **3x** was higher when measured in Vero 76 cells as compared to Calu-3 cells, showing an EC_{50} of 0.185 μM. Remdesivir and **I**, tested in the same system as control compounds, exhibited EC_{50} values of 0.0026 and 0.00958 μM, respectively. All other compounds that showed activity as antiviral agents in Calu-3 cells (**3f-h**, **3l**, **3r**, **3v**, **3w**, **3aa**, **3ae**, **3af**, and **3ah**) did not display antiviral activity in Vero 76 cells at the highest test concentration of 10 μM. This might be attributed to the poor compound permeability in Vero cells or high expression of the efflux transporter P-glycoprotein; many recent reports have revealed such variances.[48−50] Concentration−response curves for **3c**, **3i**, **3x**, remdesivir, and **I** in Vero76 cells are shown in Figure 6.

Broad-Spectrum Effect against SARS-CoV-1 M^{pro} and MERS-CoV M^{pro}. M^{pro} sequences for SARS-CoV-2, SARS-CoV-1, and MERS-CoV are known to have a high similarity in the catalytic domain, which is responsible for protein cleavage. Due to the promising M^{pro} inhibition and antiviral activity against SARS-CoV-2, we investigated the inhibitory activities of selected compounds on the main proteases of the human-pathogenic coronaviruses SARS-CoV-1 and MERS-CoV as well. Compounds were tested against recombinant SARS-CoV-1 M^{pro} and MERS-CoV M^{pro} at a high concentration of 10 μM. The classical fluorescence resonance transfer (FRET) assay was used.[51−53] Concentration-dependent inhibition curves for compounds that achieved at least 50% inhibition against the relevant M^{pro} enzyme were determined to calculate IC_{50} values (see Table 2 for IC_{50} values and Figures S13 and S14 for concentration−inhibition curves). **GC373**[54] (see Table 2) was employed as a positive control for both M^{pro} inhibitory activities.

At 10 μM, **3c**, **3h**, **3s**, **3v**, **3w**, **3x**, and **3af** displayed more than 50% inhibition of SARS-CoV-1 M^{pro}. Among all of the examined compounds, **3w** demonstrated the highest inhibitory activity, with an IC_{50} value of 0.0613 μM. **3af** had submicromolar inhibitory activity (IC_{50} 0.253 μM), whereas **3c** (IC_{50} 3.21 μM), **3f** (IC_{50} 7.35 μM), **3h** (IC_{50} 2.15 μM), **3s** (IC_{50} 2.76 μM), **3v**

https://doi.org/10.1021/acs.jmedchem.2c00636
J. Med. Chem. XXXX, XXX, XXX−XXX

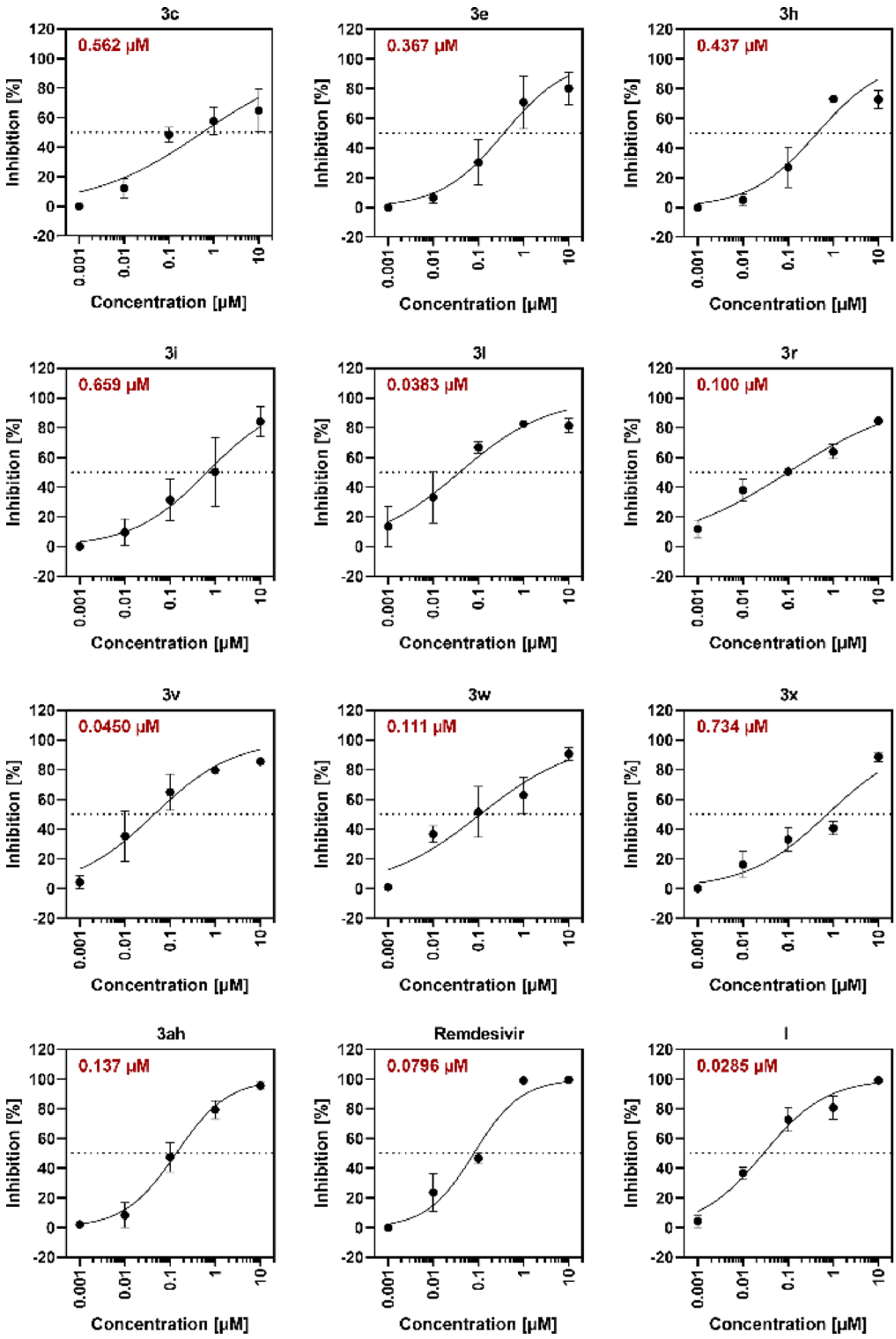

Figure 5. EC_{50} values of M^{pro} inhibitors in Calu-3 cells. Lung-derived human Calu-3 cells were incubated with 10-fold serial dilutions (10−0.001 μM) of each inhibitor or DMSO (solvent control) for 1 h followed by infection with SARS-CoV-2 at a multiplicity of infection (MOI) of 0.01. After virus inoculation, cells were further incubated with the respective inhibitors for 24 h. Supernatants were harvested, and viral titers were determined by titration on Vero E6 cells. For normalization, viral titers of DMSO-treated cells were set as 0% inhibition. Means ± SDs from three biological replicates are presented. Red numbers indicate individual EC_{50} values of the respective inhibitors.

(IC_{50} 1.65 μM), and **3y** (IC_{50} 1.52 μM) displayed inhibitory activities in the micromolar range. Compounds **3f**, **3k**, **3l**, **3ae**, and **3ah** did not inhibit SARS-CoV M^{pro}, although they did inhibit SARS-CoV-2 M^{pro}. This is possibly due to the difference in shape and size between the two M^{pro} enzymes.[55] Concentration−response curves for **3v** (IC_{50} 1.65 μM), **3w** (IC_{50} 0.0614 μM), **3x** (IC_{50} 1.52 μM), and **3af** (IC_{50} 0.253 μM) are shown in Figure S13.

We identified many compounds to inhibit the MERS-CoV M^{pro} activity in the submicromolar to nanomolar range (see

https://doi.org/10.1021/acs.jmedchem.2c00636
J. Med. Chem. XXXX, XXX, XXX−XXX

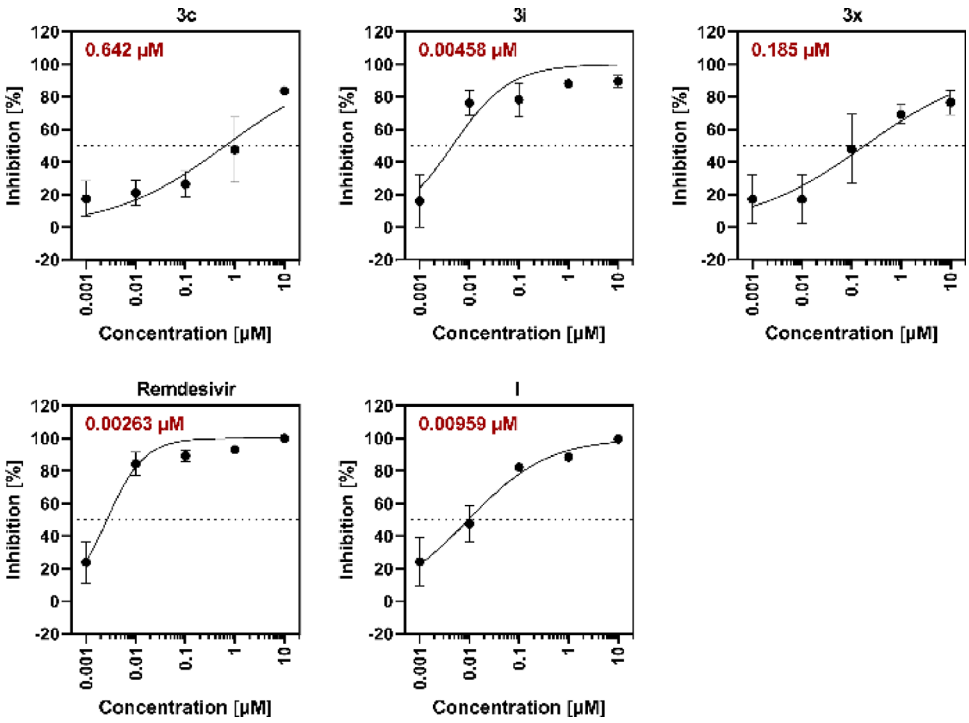

Figure 6. EC_{50} values of M^{pro} inhibitors in Vero 76 cells. Vero 76 cells were incubated with 10-fold serial dilutions (10−0.001 μM) of each inhibitor or DMSO (solvent control) for 1 h followed by infection with SARS-CoV-2 at an MOI of 0.01. After virus inoculation, cells were further incubated with the respective inhibitors for 24 h. Supernatants were harvested, and viral titers were determined by titration on Vero E6 cells. For normalization, viral titers of DMSO-treated cells were set as 0% inhibition. Means ± SDs from three biological replicates are presented. Red numbers indicate individual EC_{50} values of the respective inhibitors.

Table 2). With an IC_{50} value of 0.0792 μM, compound **3aa** was discovered to be one of the most effective representatives. The rank order of potency at MERS-CoV M^{pro} is as follows: **3aa** > **3h** > **3i** > **3g** > **3w** > **3s** > **3e** > **3l** ∼ **3v** ∼ **3c** ∼ **3af** > **3f** > **3k** ∼ **3x**. MERS-CoV M^{pro} was not inhibited by compounds **3ah** and **3ae**. Concentration−inhibition curves for **3c**, **3e**, **3f**−**i**, **3k**, **3l**, **3s**, **3v**, **3w**, **3x**, **3aa**, and **3af** are shown in Figure S14.

Thus, these thioesters represent a novel class of broad-spectrum inhibitors that target M^{pro} of SARS-CoV-1, SARS-CoV-2, and MERS-CoV, with the highest potency against SARS-CoV-2 M^{pro} followed by MERS-CoV M^{pro} and SARS-CoV-1 M^{pro}.

X-ray Structures of SARS-CoV-2 M^{pro} Bound with Inhibitors. To understand the binding interactions of the inhibitors with the protease, co-crystal structures of SARS-CoV-2 M^{pro} in complex with the broad-spectrum M^{pro} inhibitors **3w** and **3af** were determined at a resolution of 2.3, and 1.5 Å, respectively (Figure 7). Table S2 summarizes the X-ray data and refinement statistics for both complexes. Figure 7 shows that the protease-catalyzed cleavage of the inhibitors produced a thioester-type enzyme−inhibitor complex. The remaining fragment of the compounds was covalently bound to the catalytic Cys145, while the pyrimidine thiolate acted as a leaving group and departed from the active site. The indole ring of compound **3w** and the quinoline ring of **3af** mainly formed hydrophobic interactions with surrounding residues including His41, Met165, Asp187, Arg188, and Gln189 (Figure 7A,B). The catalytic His41 together with Met165 functioned as a clamp to catch the aromatic indole and quinoline ring of the inhibitors. In the complex structure of **3w** with SARS-CoV-2 M^{pro}, Met49 also contributed to the hydrophobic interactions with the indole ring, while this interaction was absent in the complex structure of **3af** due to the unclear electron density was missing in the loop where Met49 is located. The superposition of the two complex structures revealed that the quinoline of **3af** was shifted toward His41 compared to the position of the indole ring of **3w**, leading to a cooperative movement of His41 and of Met165. Such a movement of the quinoline ring might sterically clash with Met49 and thus cause a disorder of the loop containing Met49. Overall, the co-crystal structures provide a mechanistic insight into the inhibition of SARS-CoV-2 M^{pro} by two pyrimidine thioesters in which the catalytic Cys145 is acylated by the indole-carbonyl or quinolone-carbonyl group, which are well positioned in a relatively hydrophobic binding pocket.

Molecular Modeling of 3w and 3af with SARS-1-CoV M^{pro} and MERS-CoV M^{pro}. Docking studies of compounds **3w** and **3af** into M^{pro} of SARS-CoV-1 and MERS-CoV followed by short molecular dynamics (MD) simulations (5 × 200 ns) reveal a stable π−π interaction with His41 (31−58% of the analyzed simulation time) for both proteins and a specific hydrogen bond interaction between MERS-CoV M^{pro}-Q167 and the nitrogen of the indole ring for **3w**, pointing toward the solvent. Several polar contacts with the S2 pocket support the binding mode: M49, M165, and H41 (numbering of SARS-CoV-1 M^{pro}). By comparison, **3af** stabilizes a water molecule within the site, with its extra H-bond acceptor group. It is important to highlight that during our simulations, a classical force-field model was adopted that disregards potential changes in the ionization state of side chains. This is especially relevant for His41 that could further display a π-charge interaction with either the indole or the quinoline ring, yielding a more stable interaction (see Figure S15).

Glutathione Stability. We tested the stability of selected potent M^{pro} thioester inhibitors against excess glutathione

https://doi.org/10.1021/acs.jmedchem.2c00636
J. Med. Chem. XXXX, XXX, XXX−XXX

Table 2. Inhibitory Activities of Selected SARS-CoV-M^{pro} Inhibitors against Recombinant SARS-CoV-1 M^{pro} and MERS-CoV M^{pro}

compd. no.	SARS-CoV-2 M^{pro} IC_{50} (μM)	SARS-CoV-1 M^{pro} IC_{50} (μM)[a] or % inhibition at 10 μM	MERS-CoV M^{pro} IC_{50} (μM)[a] or % inhibition at 10 μM
3c	0.143 ± 0.021	3.21 ± 0.24	0.535 ± 0.032
3e	0.0600 ± 0.0257	n.d.[b,c]	0.486 ± 0.223
3f	0.0723 ± 0.0221	7.35 ± 0.93	0.945 ± 0.045
3g	0.0547 ± 0.0073	n.d.[c]	0.271 ± 0.157
3h	0.159 ± 0.038	2.15 ± 0.14	0.196 ± 0.001
3i	0.349 ± 0.123	n.d.[b]	0.223 ± 0.051
3k	0.0914 ± 0.0163	n.d.	1.13 ± 0.03
3l	0.147 ± 0.044	n.d.	0.503 ± 0.051
3s	0.250 ± 0.076	2.76 ± 0.10	0.378 ± 0.214
3v	0.454 ± 0.011	1.65 ± 0.18	0.526 ± 0.016
3w	0.0114 ± 0.0028	0.06 ± 0.00	0.303 ± 0.059
3x	0.0876 ± 0.0109	1.52 ± 0.01	1.31 ± 0.28
3aa	0.0181 ± 0.0039	n.d.[c]	0.0790 ± 0.0280
3ae	0.0144 ± 0.0020	n.d.[b]	n.d.
3af	0.0206 ± 0.0006	0.253 ± 0.163	0.613 ± 0.155
3ah	0.117 ± 0.048	n.d.	n.d.
GC373[d]	n.d.	0.0446 ± 0.0020	0.0780 ± 0.0170

[a]IC_{50} values represent the average of two independent experiments determined in triplicate. Errors are given by the ratio between the standard deviation and the square root of the number of measurements. [b]n.d.: not determined. [c]Compounds **3e**, **3g**, and **3aa** displayed high fluorescence in the SARS-CoV-1 M^{pro} assay, interfering with the measurement of the enzymatic activity readout and hindering the evaluation of their potency in our assay. [d]GC373 = ((2*S*)-2-((*S*)-2-(((benzyloxy)carbonyl)amino)-4-methylpentanamido)-3-(2-oxopyrrolidin-3-yl)propanal).

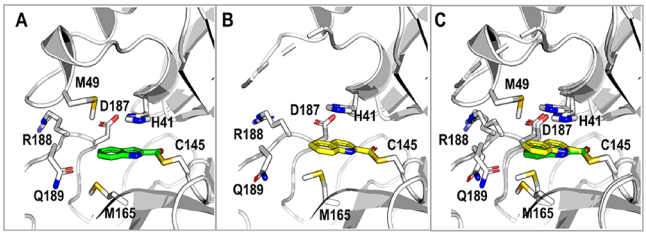

Figure 7. Binding modes of (A) **3w** (PDB ID: 7X6K) and (B) **3af** (PDB ID: 7X6J) with SARS-CoV-2 M^{pro} revealed by co-crystal structures. The protease is shown in gray cartoon, **3w** in green sticks, **3af** in yellow sticks, and the surrounding residues in light gray sticks. (C) A superposition of **3w** (green) and **3af** (yellow) bound with the protease shows the different conformational perturbations at the active site caused by the binding of the inhibitors.

(GSH) as a physiological nucleophile to identify the inherent activity toward thiols under physiological conditions. These experiments revealed that inhibitors are stable with low inherent activity under the assay conditions (5 mM GSH at pH 7.4) (see a representative example, **3an**, in Figure S16). This indicates that the M^{pro} inhibition of thioesters is dependent not on their chemical reactivity toward GSH but rather on the specific reactivity toward catalytic Cys145 at the active site of M^{pro}, as shown by the X-ray structures of SARS-CoV-2 M^{pro} bound with inhibitors in Figure 7.

CONCLUSIONS

The M^{pro} of SARS-CoV-2 is an important target since it is involved in the coronavirus life cycle. We developed, synthesized, and tested novel low-molecular-weight thioesters that act as inhibitors of M^{pro} of SARS-CoV-2, the virus that is causing the current COVID-19 pandemic. A number of compounds showed low nanomolar M^{pro} inhibitory activity with an irreversible inhibition mechanism. The co-crystal structure of M^{pro} with **3a** and **3af**, two of the most potent inhibitors, validated the proposed binding mechanism. In cell-based experiments, several compounds exhibited excellent antiviral activity. The SARS-CoV-2 M^{pro} inhibitors were additionally shown to inhibit M^{pro} of the related pathogenic coronaviruses SARS-CoV-1 and MERS-CoV, indicating that they are potential candidates for further development as broad-spectrum anti-coronaviral agents.

EXPERIMENTAL SECTION

General Experimental Procedures. All commercially available reagents and solvents were used as received. Reactions sensitive to air or moisture were performed under an atmosphere of argon and/or in anhydrous solvents. Anhydrous solvents were purchased from Acros Organics (AcroSeal). Unless stated otherwise, extracts were dried over sodium sulfate prior to filtration. Thin-layer chromatography was performed on TLC Silica Gel 60F254 aluminum sheets provided by Merck, with detection at 254 and 366 nm. Flash chromatography was carried out on an Interchim PuriFlash XS420 flash chromatography system and Grace Davison Davisil LC60A 20e45 mm silica or Merck Geduran Si60 63−200 μm. Mass spectra were recorded on an Advion DCMS interface (ESI voltage: 3.50 kV, capillary voltage: 187 V, source voltage: 44 V, capillary temperature: 250 °C, desolvation gas temperature: 250 °C, gas flow rate: 5 L/min N_2), with elution of the spots with MeOH. High-resolution mass spectrometry (HRMS) for the final compound was measured by the mass spectrometry department, Institute of Organic Chemistry, Eberhard Karls University Tuebingen, on a Bruker maXis 4G ESI-TOF instrument. The instrument was run in ESI+ mode, and the settings were as follows: nebulizer gas of 1.2 bar, gas flow of 6.0 L/min, source temperature of 200 °C, capillary voltage of 4500 V, endplate offset of −500 V, and m/z range from 80 to 1000. NMR spectra were measured on Bruker Avance 400 or 600 NMR spectrometers. The spectra were calibrated on the deuterated solvents, and chemical shifts (d) are stated relative to tetramethylsilane in ppm. The solvent used was deuterated chloroform (d_3) and deuterated DMSO (d_6). Melting points were measured on a melting point apparatus (Mettler Toledo MP70, hand method, temperature from 60 to 360 °C, heating rate 20.0 °C/min) and are uncorrected.

The purity of the final compound was determined via high-performance liquid chromatography (HPLC) using an Agilent 1100 Series LC system (Agilent Technologies, Santa Clara, CA) with a Phenomenex Kinetex C8 100A column (150 mm × 4.6 mm, 2.6 μm) (Phenomenex Inc., Torrance, CA), and detection was performed with a UV DAD at a wavelength of 254 nm. Elution was carried out with the following gradients: 0.01 M KH2PO4 (pH 2.32) (solvent A) and MeOH (solvent B). Method A was follows: 0 min, 40% B/60% A; 9 min, 95% B/5% A; 10 min, 95% B/5% A; 11 min, 40% B/60% A; and 16 min, 40% B/60% A, with a flow of 0.5 mL/min. Method B was follows: 0 min, 40% B/60% A; 15 min, 85% B/15% A; 20 min, 85% B/15% A; 22 min, 40% B/60% A; and 28 min, 40% B/60% A, with a flow 0.5 mL/min. The final compounds showed a purity of >95% according to the peak areas.

Synthesis of Thioesters 3a−z and 3aa−an. $POCl_3$ (1.37 mmol, 1.1 equiv) was added to a solution of pyridine (1.37 mmol, 1.1 equiv) and corresponding carboxylic acids (**1a−s**, 1.25 mmol, 1.0 equiv) in dry DCM (10 mL), and the solution was stirred for 10−15 min at room temperature to generate carboxylic acid chlorides in situ. The appropriate thiols (**2a−n**) were added first followed by pyridine (2.0 mmol, 1.6 equiv). TLC with UV detection was used to monitor the

https://doi.org/10.1021/acs.jmedchem.2c00636
J. Med. Chem. XXXX, XXX, XXX−XXX

reaction. The mixture was put into ice water and extracted with DCM (2 × 25 mL) when the reaction was completed after 12 h. After washing with 1 N HCl (20 mL) and 30−40% NaOH solutions, the combined organic layers were brined (20 mL). The solution was then dried over Na_2SO_4, filtered, and evaporated until it was completely dry. The resulting residue was purified by silica gel chromatography using 10−20% EtOAc in hexane to afford the desired products.

S-(4-Chlorophenyl)-1H-indole-2-carbothioate (3a). The product **3a** was synthesized from the reaction of indole-2-carboxylic acid (**1a**, 201 mg, 1.25 mmol) and 4-chlorobenzenethiol (**2a**, 180.7 mg, 1.25 mmol) in the presence of pyridine (0.11 mL, 1.1 equiv; 0.161 mL, 1.6 equiv). Light yellow solid; yield 78% (279 mg); Mp: 230−232 °C. ^{1}H NMR (400 MHz, DMSO-d_6) δ 12.11 (s, 1H, NH), 7.74 (d, J = 8.0 Hz, 1H), 7.59 (s, 4H), 7.51−7.45 (m, 2H), 7.35−7.30 (m, 1H), 7.16−7.10 (m, H). ^{13}C NMR (101 MHz, DMSO-d_6) δ 180.66, 138.39, 137.18, 135.27, 133.23, 129.89, 127.13, 126.42, 125.97, 123.12, 121.23, 113.32, 109.14. HRMS (ESI-TOF) m/z for ($C_{15}H_{10}ClNOS$ [M + Na]$^+$) calcd 310.0069, found 310.0067. HPLC t_R = 9.581 min.

S-(2,4-Dichlorophenyl)-1H-indole-2-carbothioate (3b). The product **3b** was synthesized from the reaction of indole-2-carboxylic acid (**1a**, 201 mg, 1.25 mmol) and 2,4-dichlorobenzenethiol (**2b**, 224 mg, 1.25 mmol) in the presence of pyridine (0.11 mL, 1.1 equiv; 0.161 mL, 1.6 equiv). Light yellow solid; yield 69% (278 mg); Mp: 225−227 °C. ^{1}H NMR (400 MHz, DMSO-d_6) δ 12.15 (s, 1H, NH), 7.92 (d, J = 2.2 Hz, 1H), 7.77 (t, J = 8.1 Hz, 2H), 7.70−7.55 (m, 2H), 7.48 (dd, J = 8.4, 0.7 Hz, 1H), 7.41−7.30 (m, 1H), 7.25−7.02 (m, 1H). ^{13}C NMR (101 MHz, DMSO-d_6) δ 179.07, 139.83, 139.53, 138.47, 136.55, 132.87, 130.31, 128.75, 127.11, 126.65, 125.55, 123.22, 121.34, 113.34, 109.68. HRMS (ESI-TOF) m/z for ($C_{15}H_9Cl_2NOS$ [M + Na]$^+$) calcd 343.9680, found 343.9678. HPLC t_R = 10.675 min.

S-(1,3,4-Thiadiazol-2-yl)-1H-indole-2-carbothioate (3c). The product **3c** was synthesized from the reaction of indole-2-carboxylic acid (**1a**, 201 mg, 1.25 mmol) and 1,3,4-thiadiazole-2-thiol (**2c**, 147 mg, 1.25 mmol) in the presence of pyridine (0.110 mL, 1.1 equiv; 0.161 mL, 1.6 equiv). White solid; yield 80% (261 mg); Mp: 192−194 °C. ^{1}H NMR (400 MHz, DMSO-d_6) δ 12.40 (s, 1H), 9.88 (s, 1H), 7.78 (d, J = 8.1 Hz, 1H), 7.72 (d, J = 1.4 Hz, 1H), 7.51 (d, J = 8.4 Hz, 1H), 7.40 (t, J = 7.6 Hz, 1H), 7.18 (t, J = 7.5 Hz, 1H). ^{13}C NMR (101 MHz, DMSO-d_6) δ 176.19, 162.95, 157.81, 137.36, 128.50, 126.99, 124.46, 122.10, 120.13, 112.63, 107.49. HRMS (ESI-TOF) m/z for ($C_{11}H_7N_3OS_2$ [M + Na]$^+$) calcd 283.9929, found. 283.9924. HPLC t_R = 6.848 min.

S-(5-Methyl-1,3,4-thiadiazol-2-yl)-1H-indole-2-carbothioate (3d). The product **3d** was synthesized from the reaction of indole-2-carboxylic acid (**1a**, 201 mg, 1.25 mmol) and 5-methyl-1,3,4-thiadiazole-2-thiol (**2d**, 165 mg, 1.25 mmol) in the presence of pyridine (0.110 mL, 1.1 equiv; 0.161 mL, 1.6 equiv). Light yellow solid; yield 59% (203 mg); Mp: 183−185 °C. ^{1}H NMR (400 MHz, $CDCl_3$) δ 9.04 (s, 1H), 7.76 (d, J = 8.0 Hz, 1H), 7.51 (d, J = 1.6 Hz, 1H), 7.48−7.39 (m, 2H), 7.22 (t, 1H), 2.87 (s, 3H). ^{13}C NMR (101 MHz, $CDCl_3$) δ 177.26, 168.28, 156.51, 137.84, 131.87, 127.72, 127.35, 123.52, 122.00, 112.39, 111.08, 15.81. (ESI-TOF) m/z for ($C_{12}H_9N_3OS_2$ [M + Na]$^+$) calcd 298.0085, found 298,0080. HPLC t_R = 7.268 min.

S-(5-Methyl-1,3,4-thiadiazol-2-yl)-1H-indole-4-carbothioate (3e). The product **3e** was synthesized from the reaction of indole-4-carboxylic acid (**1b**, 201 mg, 1.25 mmol) and 5-methyl-1,3,4-thiadiazole-2-thiol (**2d**, 165 mg, 1.25 mmol) in the presence of pyridine (0.110 mL, 1.1 equiv; 0.161 mL, 1.6 equiv). Brown solid; yield 63% (216 mg); Mp: 152−154 °C. ^{1}H NMR (400 MHz, DMSO-d_6) δ 11.77 (s, 1H), 8.07−7.84 (m, 2H), 7.70 (t, J = 2.8 Hz, 1H), 7.34 (t, J = 7.8 Hz, 1H), 6.98 (t, J = 2.1 Hz, 1H), 2.84 (s, 3H). ^{13}C NMR (101 MHz, DMSO-d_6) δ 184.88, 169.26, 157.35, 137.35, 130.55, 125.80, 125.33, 122.62, 121.22, 119.68, 102.12, 15.74. HRMS (ESI-TOF) m/z for ($C_{12}H_9N_3OS_2$ [M + Na]$^+$) calcd 298.0085, found 298. 0079. HPLC t_R = 6.364 min.

S-(5-Methyl-1,3,4-thiadiazol-2-yl)-1H-indole-5-carbothioate (3f). The product **3f** was synthesized from the reaction of indole-5-carboxylic acid (**1c**, 201 mg, 1.25 mmol) and 5-methyl-1,3,4-thiadiazole-2-thiol (**2d**, 165 mg, 1.25 mmol) in the presence of pyridine (0.110 mL, 1.1 equiv; 0.161 mL, 1.6 equiv). Brown solid; yield 61% (210 mg); Mp: 179−181 °C. ^{1}H NMR (400 MHz, DMSO-d_6) δ 11.76 (s, 1H), 8.42 (s, 1H), 7.76 (d, J = 1.6 Hz, 1H), 7.71−7.34 (m, 2H), 6.73 (s, 1H), 2.83 (s, 3H). ^{13}C NMR (101 MHz, DMSO-d_6) δ 187.81, 169.07, 138.44, 127.96, 127.22, 123.31, 122.40, 111.24, 102.95, 15.65. HRMS (ESI-TOF) m/z for ($C_{12}H_9N_3OS_2$ [M + Na]$^+$) calcd 298.0085, found 298.0079. HPLC t_R = 7.411 min.

S-(5-Methyl-1,3,4-thiadiazol-2-yl)-1H-indole-6-carbothioate (3g). The product **3g** was synthesized from the reaction of indole-6-carboxylic acid (**1d**, 201 mg, 1.25 mmol) and 5-methyl-1,3,4-thiadiazole-2-thiol (**2d**, 165 mg, 1.25 mmol) in the presence of pyridine (0.110 mL, 1.1 equiv; 0.161 mL, 1.6 equiv). Light yellow solid; yield 60% (206 mg); Mp: 186−188 °C. ^{1}H NMR (400 MHz, DMSO-d_6) δ 11.74 (s, 1H), 8.18−8.16 (m, 1H), 7.78−7.74 (d, J = 6.6, 3.6 Hz, 2H), 7.67 (dd, J = 8.4, 1.7 Hz, 1H), 6.64−6.62 (dd, J = 2.8, 1.8 Hz, 1H), 2.82 (s, 3H). ^{13}C NMR (101 MHz, DMSO-d_6) δ 185.16, 169.98, 168.85, 165.79, 135.64, 131.52, 129.36, 123.58, 120.25, 120.06, 113.99, 101.92, 16.04. HRMS (ESI-TOF) m/z for ($C_{12}H_9N_3OS_2$ [M + Na]$^+$) calcd 298.0085, found 298.0080. HPLC t_R = 7.197 min.

S-(5-Methyl-1,3,4-thiadiazol-2-yl)-1H-indole-7-carbothioate (3h). The product **3h** was synthesized from the reaction of indole-6-carboxylic acid (**1e**, 201 mg, 1.25 mmol) and 5-methyl-1,3,4-thiadiazole-2-thiol (**2d**, 165 mg, 1.25 mmol) in the presence of pyridine (0.110 mL, 1.1 equiv; 0.161 mL, 1.6 equiv). Light brown solid; yield 47% (161 mg); Mp: 180−182 °C. ^{1}H NMR (400 MHz, $CDCl_3$) δ 11.57 (s, 1H), 8.04 (dd, J = 21.8, 7.6 Hz, 2H), 7.46 (s, 1H), 7.26 (d, J = 7.7 Hz, 1H), 6.65 (s, 1H), 2.85 (s, 3H). ^{13}C NMR (101 MHz, $CDCl_3$) δ 186.01, 168.16, 157.09, 133.76, 129.80, 128.97, 126.25, 123.62, 119.53, 117.90, 103.06, 15.68. HRMS (ESI-TOF) m/z for ($C_{12}H_9N_3OS_2$ [M + Na]$^+$) calcd 298.0085, found 298.0080. HPLC t_R = 7.636 min.

S-(5-Methyl-1,3,4-thiadiazol-2-yl)-1-methyl-1H-indole-2-carbothioate (3i). The product **3i** was synthesized from the reaction of 1-methyl-1*H*-indole-2-carboxylic acid (**1f**, 219 mg, 1.25 mmol) and 5-methyl-1,3,4-thiadiazole-2-thiol (**2d**, 165 mg, 1.25 mmol) in the presence of pyridine (0.110 mL, 1.1 equiv; 0.161 mL, 1.6 equiv). Yellow solid; yield 68% (246 mg); Mp: 171−173 °C. ^{1}H NMR (400 MHz, $CDCl_3$) δ 7.81 (d, J = 8.9 Hz, 2H), 7.67 (d, J = 8.1 Hz, 1H), 7.51−7.43 (m, 1H), 7.23 (t, J = 7.3 Hz, 1H), 4.02 (d, J = 6.7 Hz, 3H), 2.84 (s, 3H). ^{13}C NMR (101 MHz, $CDCl_3$) δ 177.61, 168.05, 157.17, 140.70, 131.76, 127.21, 125.89, 123.32, 121.55, 112.72, 110.52, 32.06, 15.64. HRMS (ESI-TOF) m/z for ($C_{13}H_{11}N_3OS_2$ [M + Na]$^+$) calcd 312.0242, found 312.0235. HPLC t_R = 8.553 min.

S-(5-(Trifluoromethyl)-1,3,4-thiadiazol-2-yl)-1H-indole-2-carbothioate (3j). The product **3j** was synthesized from the reaction of indole-2-carboxylic acid (**1a**, 201 mg, 1.25 mmol) and 5-(trifluoromethyl)-1,3,4-thiadiazole-2-thiol (**2e**, 233 mg, 1.25 mmol) in the presence of pyridine (0.110 mL, 1.1 equiv; 0.161 mL, 1.6 equiv). Yellow solid; yield 71% (292 mg); Mp: 209−211 °C. ^{1}H NMR (400 MHz, DMSO-d_6) δ 11.75 (s, 1H), 7.64 (t, J = 7.0 Hz, 1H), 7.44 (dd, J = 8.3, 0.9 Hz, 1H), 7.24 (dd, J = 8.2, 7.0 Hz, 1H), 7.16−6.97 (m, 2H). ^{13}C NMR (101 MHz, DMSO-d_6) δ 163.26, 137.70, 128.11 (d, J = 154.8 Hz), 127.32, 124.73, 122.40, 120.42, 112.95, 107.75. HRMS (ESI-TOF) m/z for ($C_{13}H_6F_3N_3OS_2$ [M + Na]$^+$) calcd 351.9802, found. 351.9798. HPLC t_R = 9.212 min.

S-(5-(Methylthio)-1,3,4-thiadiazol-2-yl)-1H-indole-2-carbothioate (3k). The product **3k** was synthesized from the reaction of indole-2-carboxylic acid (**1a**, 201 mg, 1.25 mmol) and 5-(methylthio)-1,3,4-thiadiazole-2-thiol (**2f**, 205 mg, 1.25 mmol) in the presence of pyridine (0.110 mL, 1.1 equiv; 0.161 mL, 1.6 equiv). White solid; yield 73% (280 mg); Mp: 186−188 °C. ^{1}H NMR (400 MHz, DMSO-d_6) δ 12.06 (s, 1H), 7.79 (t, J = 8.1 Hz, 1H), 7.67 (dd, J = 8.8, 2.35 Hz, 2H), 7.60−7.48 (m, 1H), 7.47−7.32 (m, 2H), 2.80 (s, 3H). ^{13}C NMR (101 MHz, DMSO-d_6) δ 176.65, 171.45, 163.26, 155.51, 139.12, 137.70, 131.82, 127.50, 124.75, 122.41, 120.43, 113.48, 111.43, 107.78, 16.82. HRMS (ESI-TOF) m/z for ($C_{12}H_9N_3OS_3$ [M + Na]$^+$) calcd 329.9806, found 329.9801. HPLC t_R = 8.267 min.

S-(5-Methoxy-1,3,4-thiadiazol-2-yl)-1H-indole-2-carbothioate (3l). The product **3l** was synthesized from the reaction of indole-2-carboxylic acid (**1a**, 201 mg, 1.25 mmol) and 5-methoxy-1,3,4-thiadiazole-2-thiol (**2 g**, 185 mg, 1.25 mmol) in the presence of pyridine (0.110 mL, 1.1 equiv; 0.161 mL, 1.6 equiv). Yellow solid; yield 53% (193 mg); Mp: 167−169 °C. ^{1}H NMR (400 MHz, DMSO-d_6) δ

https://doi.org/10.1021/acs.jmedchem.2c00636
J. Med. Chem. XXXX, XXX, XXX−XXX

12.35 (s, 1H), 7.77 (d, J = 8.1 Hz, 1H), 7.66 (d, J = 1.5 Hz, 1H), 7.50 (d, J = 8.4 Hz, 1H), 7.44−7.29 (m, 1H), 7.17 (t, J = 7.5 Hz, 1H), 4.22 (s, 3H). HRMS (ESI-TOF) m/z for ($C_{12}H_9N_3O_2S_2$ [M + Na]$^+$) calcd 314.0034, found 314.0031. HPLC t_R = 8.885 min.

*S-(5-Ethoxy-1,3,4-thiadiazol-2-yl)-1H-indole-2-carbothioate (**3m**).* The product **3m** was synthesized from the reaction of indole-2-carboxylic acid (**1a**, 201 mg, 1.25 mmol) and 5-ethoxy-1,3,4-thiadiazole-2-thiol (**2h**, 206 mg, 1.25 mmol) in the presence of pyridine (0.110 mL, 1.1 equiv; 0.161 mL, 1.6 equiv). Yellow solid; yield 63% (240 mg); Mp: 185−187 °C. ^{1}H NMR (400 MHz, $CDCl_3$) δ 8.88 (s, 1H), 7.68 (d, J = 7.9 Hz, 1H), 7.35 (dd, J = 12.6, 6.1 Hz, 3H), 7.15 (dd, J = 10.7, 3.9 Hz, 1H), 4.58 (q, J = 7.1 Hz, 2H), 1.44 (t, J = 7.1 Hz, 3H). ^{13}C NMR (101 MHz, $CDCl_3$) δ 177.84, 176.97, 162.94, 148.80, 137.35, 128.51, 126.98, 124.45, 122.09, 120.13, 112.62, 107.48, 70.35, 14.29. HRMS (ESI-TOF) m/z for ($C_{13}H_{11}N_3O_2S_2$ [M + Na]$^+$) calcd 328.0191, found 328.01860. HPLC t_R = 8.885 min.

*S-(5-Methyl-1,3,4-oxadiazol-2-yl)-1H-indole-2-carbothioate (**3n**).* The product **3n** was synthesized from the reaction of indole-2-carboxylic acid (**1a**, 201 mg, 1.25 mmol) and 5-methyl-1,3,4-oxadiazole-2-thiol (**2i**, 145 mg, 1.25 mmol) in the presence of pyridine (0.110 mL, 1.1 equiv; 0.161 mL, 1.6 equiv). Brown solid; yield 60% (195 mg); Mp: 218−220 °C. ^{1}H NMR (400 MHz, DMSO-d_6) δ 12.14 (s, 1H), 7.74 (d, J = 7.9 Hz, 1H), 7.68 (s, 1H), 7.51 (d, J = 8.1 Hz, 1H), 7.35 (t, J = 7.3 Hz, 1H), 7.12 (t, J = 7.2 Hz, 1H), 2.50 (s, 3H). ^{13}C NMR (101 MHz, DMSO-d_6) δ 175.09, 159.99, 157.06, 138.85, 127.25, 127.23, 126.98, 123.58, 121.31, 114.77, 113.25, 11.58. HRMS (ESI-TOF) m/z for ($C_{12}H_9N_3O_2S$ [M + Na]$^+$) calcd 282.0313, found 282.0306. HPLC t_R = 7.048 min.

*S-(4-(1H-Indole-2-carbonyl)-5-methyl-4H-1,2,4-triazol-3-yl)1H-indole-2-carbothioate (**3o**).* The product **3o** was synthesized from the reaction of indole-2-carboxylic acid (**1a**, 201 mg, 1.25 mmol) and 5-methyl-4H-1,2,4-triazole-3-thiol (**2j**, 144 mg, 1.25 mmol) in the presence of pyridine (0.110 mL, 1.1 equiv; 0.161 mL, 1.6 equiv). Light yellow solid; yield 45% (112 mg); Mp: 227−229 °C. ^{1}H NMR (400 MHz, $CDCl_3$) δ 10.35 (s, 1H), 8.93 (s, 1H), 7.86 (d, J = 1.0 Hz, 1H), 7.69 (dd, J = 7.9, 3.3 Hz, 2H), 7.51−7.42 (m, 2H), 7.42−7.27 (m, 3H), 7.18−7.02 (m, 2H), 2.89 (d, J = 8.3 Hz, 3H). ^{13}C NMR (101 MHz, DMSO-d_6) δ 178.33, 159.75, 158.27, 152.17, 139.05, 138.81, 132.63, 127.32, 126.98, 123.79121.47, 121.34, 115.79, 113.30, 110.56, 15.99. HRMS (ESI-TOF) m/z for ($C_{21}H_{15}N_5O_2S$ [M + Na]$^+$) calcd 424.0844, found 428.0842. HPLC t_R = 7.102 min.

*S-(5-Methyl-1,3,4-thiadiazol-2-yl)benzofuran-2-carbothioate (**3p**).* The product **3p** was synthesized from the reaction of benzofuran-2-carboxylic acid (**1g**, 203 mg, 1.25 mmol) and 5-methyl-1,3,4-thiadiazole-2-thiol (**2d**, 165 mg, 1.25 mmol) in the presence of pyridine (0.110 mL, 1.1 equiv; 0.161 mL, 1.6 equiv). Yellow solid; yield 74% (255 mg); Mp: 156−158 °C. ^{1}H NMR (400 MHz, $CDCl_3$) δ 7.70 (d, J = 7.9 Hz, 1H), 7.65 (s, 1H), 7.58 (d, J = 8.5 Hz, 1H), 7.54−7.43 (m, 1H), 7.31 (t, J = 7.5 Hz, 1H), 2.81 (s, 3H). ^{13}C NMR (101 MHz, $CDCl_3$) δ 176.02, 168.20, 156.04, 129.37, 126.69, 124.64, 123.63, 113.87, 112.67, 15.64. HRMS (ESI-TOF) m/z for ($C_{12}H_8N_2O_2S_2$ [M + Na]$^+$) calcd 298.9925, found 298.9918. HPLC t_R = 9.212 min.

*S-(5-Methyl-1,3,4-thiadiazol-2-yl)-5-bromofuran-2-carbothioate (**3q**).* The product **3q** was synthesized from the reaction of 5-bromofuran-2-carboxylic acid (**1h**, 237 mg, 1.25 mmol) and 5-methyl-1,3,4-thiadiazole-2-thiol (**2d**, 165 mg, 1.25 mmol) in the presence of pyridine (0.110 mL, 1.1 equiv; 0.161 mL, 1.6 equiv). Light brown solid; yield 66% (252 mg); Mp: 185−187 °C. ^{1}H NMR (400 MHz, $CDCl_3$) δ 7.81 (d, J = 3.8 Hz, 1H), 7.05 (s, 1H), 2.83 (s, 3H). ^{13}C NMR (101 MHz, $CDCl_3$) δ 172.84, 168.39, 150.41, 130.35, 120.31, 115.32, 15.65. HRMS (ESI-TOF) m/z for ($C_8H_5BrN_2O_2S_2$ [M + Na]$^+$) calcd 326.8874, found 326.8866. HPLC t_R = 5.845 min.

*S-(5-Methyl-1,3,4-thiadiazol-2-l)-5-phenylfuran-2-carbothioate (**3r**).* The product **3r** was synthesized from the reaction of 5-phenylfuran-2-carboxylic acid (**1i**, 235 mg, 1.25 mmol) and 5-methyl-1,3,4-thiadiazole-2-thiol (**2d**, 165 mg, 1.25 mmol) in the presence of pyridine (0.110 mL, 1.1 equiv; 0.161 mL, 1.6 equiv). Light yellow solid; yield 58% (219 mg). ^{1}H NMR (400 MHz, $CDCl_3$) δ 7.85−7.70 (m, 2H), 7.50−7.31 (m, 4H), 6.82 (d, J = 3.8 Hz, 1H), 2.80 (s, 3H). ^{13}C NMR (101 MHz, $CDCl_3$) δ 168.24, 160.33, 159.57, 156.73, 130.04, 129.12, 126.00, 125.47, 125.24, 120.64, 108.14. 15.36. HRMS (ESI-TOF) m/z for ($C_{14}H_{10}N_2O_2S_2$ [M + Na]$^+$) calcd 325.0081, found 325.0075. HPLC t_R = 8.305 min.

*S-(5-Methyl-1,3,4-thiadiazol-2-l)-5-(phenylethynyl)furan-2-carbothioate (**3s**).* The product **3s** was synthesized from the reaction of 5-(phenylethynyl)furan-2-carboxylic acid (**1j**, 265 mg, 1.25 mmol) and 5-methyl-1,3,4-thiadiazole-2-thiol (**2d**, 165 mg, 1.25 mmol) in the presence of pyridine (0.110 mL, 1.1 equiv; 0.161 mL, 1.6 equiv). Light yellow solid; yield 70% (286 mg); Mp: 177−179 °C. ^{1}H NMR (400 MHz, $CDCl_3$) δ 7.52 (dd, J = 7.6, 1.5 Hz, 2H), 7.46−7.26 (m, 4H), 6.74 (d, J = 3.7 Hz, 1H), 2.79 (s, 3H). ^{13}C NMR (101 MHz, $CDCl_3$) δ 173.29, 168.14, 156.04, 148.42, 142.04, 131.89, 129.86, 128.62, 120.96, 119.17, 117.39, 96.86, 78.18, 15.63. HRMS (ESI-TOF) m/z for ($C_{16}H_{10}N_2O_2S_2$ [M + Na]$^+$) calcd 349.0082, found 349.0075. HPLC t_R = 8.718 min.

*S-(5-(Trifluoromethyl)-1,3,4-thiadiazol-2-l)-5-(phenylethynyl)-furan-2-carbothioate (**3t**).* The product **3t** was synthesized from the reaction of 5-(phenylethynyl)furan-2-carboxylic acid (**1j**, 265 mg, 1.25 mmol) and 5-(trifluoromethyl)-1,3,4-thiadiazole-2-thiol (**2e**, 233 mg, 1.25 mmol) in the presence of pyridine (0.110 mL, 1.1 equiv; 0.161 mL, 1.6 equiv). Light yellow solid; yield 76% (361 mg); Mp: 131−133 °C. ^{1}H NMR (400 MHz, DMSO-d_6) δ 7.66−7.59 (m, 2H), 7.53−7.45 (m, 3H), 7.32 (d, J = 3.6 Hz, 1H), 7.07 (d, J = 3.6 Hz, 1H). ^{13}C NMR (101 MHz, DMSO-d_6) δ 170.86, 160.80, 157.77 (t, J = 39.3 Hz), 146.73, 141.78, 130.92, 129.04, 127.64, 119.72, 119.21, 117.27, 116.05 (d, J = 121.8 Hz), 115.45, 96.48, 76.94. HRMS (ESI-TOF) m/z for ($C_{16}H_7F_3N_2O_2S_2$ [M + Na]$^+$) calcd 402.9799, found 402.9790, HPLC t_{ret} = 8.307 min.

*(5-Methyl-2-thioxo-1,3,4-thiadiazol-3(2H)-yl)-(5-phenyl-1H-pyrrol-2-yl)ethanone (**3u**).* The product **3u** was synthesized from the reaction of 5-phenyl-1H-pyrrole-2-carboxylic acid (**1k**, 233 mg, 1.25 mmol) and 5-methyl-1,3,4-thiadiazole-2-thiol (**2d**, 165 mg, 1.25 mmol) in the presence of pyridine (0.110 mL, 1.1 equiv; 0.161 mL, 1.6 equiv). Yellow solid; yield 68% (262 mg); Mp: 199−201 °C. ^{1}H NMR (400 MHz, $CDCl_3$) δ 9.65 (s, 1H), 7.53 (d, J = 7.4 Hz, 2H), 7.37 (s, 2H), 7.32 (t, J = 7.3 Hz, 1H), 7.15 (dd, J = 3.9, 2.4 Hz, 1H), 6.72−6.45 (m, 1H), 2.49 (s, 3H). HRMS (ESI-TOF) m/z for ($C_{14}H_{11}N_3OS_2$ [M + Na]$^+$) calcd 324.0242, found 324,0234. HPLC t_R = 7.414 min.

*S-(5-Methyl-1,3,4-thiadiazol-2-yl)naphthalene-2-carbothioate (**3v**).* The product **3v** was synthesized from the reaction of 2-naphthoic acid (**1l**, 215 mg, 1.25 mmol) and 5-methyl-1,3,4-thiadiazole-2-thiol (**2d**, 165 mg, 1.25 mmol) in the presence of pyridine (0.110 mL, 1.1 equiv; 0.161 mL, 1.6 equiv). Light yellow crystalline solid; yield 82% (295 mg); Mp: 167−169 °C. ^{1}H NMR (400 MHz, $CDCl_3$) δ 8.52 (s, 1H), 7.94 (dd, J = 8.3, 1.1 Hz, 1H), 7.92−7.87 (m, 1H), 7.88−7.75 (m, 2H), 7.59 (dd, J = 8.2, 6.9 Hz, 1H), 7.54 (dd, J = 8.1, 7.0 Hz, 1H), 2.80 (s, 3H). ^{13}C NMR (101 MHz, $CDCl_3$) δ 185.71, 167.96, 157.29, 136.36, 132.37, 129.90, 129.81, 129.50, 129.25, 127.98, 127.52, 122.86, 15.64. HRMS (ESI-TOF) m/z for ($C_{14}H_{10}N_2OS_2$ [M + Na]$^+$) calcd 309.0133, found 309.0129. HPLC t_R = 9.581 min.

*S-(Pyrimidin-2-yl)-1H-indole-2-carbothioate (**3w**).* The product **3w** was synthesized from the reaction of indole-2-carboxylic acid (**1a**, 201 mg, 1.25 mmol) and pyrimidine-2-thiol (**2k**, 140 mg, 1.25 mmol) in the presence of pyridine (0.110 mL, 1.1 equiv; 0.161 mL, 1.6 equiv). Yellow solid; yield 79% (252 mg); Mp: 156−158 °C. ^{1}H NMR (400 MHz, DMSO-d_6) δ 12.14 (s, 1H), 8.94 (dd, J = 7.7, 3.3 Hz, 2H), 7.76 (d, J = 8.1 Hz, 1H), 7.60 (s, 1H), 7.50 (dd, J = 9.3, 5.3 Hz, 2H), 7.35 (dd, J = 8.3, 7.0 Hz, 1H), 7.30−6.87 (m, 1H). ^{13}C NMR (101 MHz, DMSO-d_6) δ 179.14, 164.12, 159.52, 138.73, 133.43, 127.06, 126.73, 123.30, 121.39, 121.34, 113.36, 110.08. HRMS (ESI-TOF) m/z for ($C_{13}H_9N_3OS$ [M + Na]$^+$) calcd 278.0364, found 278.0357. HPLC t_R = 6.811 min.

*S-(4-Methylpyrimidin-2-yl)-1H-indole-2-carbothioate (**3x**).* The product **3x** was synthesized from the reaction of indole-2-carboxylic acid (**1a**, 201 mg, 1.25 mmol) and 4-methyl pyrimidine-2-thiol (**2l**, 157 mg, 1.25 mmol) in the presence of pyridine (0.110 mL, 1.1 equiv; 0.161 mL, 1.6 equiv). Yellow solid; yield 84% (282 mg); Mp: 156−158 °C. ^{1}H NMR (400 MHz, DMSO-d_6) δ 12.13 (s, 1H), 8.78 (d, J = 5.0 Hz, 1H), 7.76 (d, J = 8.0 Hz, 1H), 7.70−7.41 (m, 2H), 7.42−7.21 (m, 1H), 7.30−6.83 (m, 2H), 2.53 (d, J = 8.0 Hz, 3H). ^{13}C NMR (101 MHz,

https://doi.org/10.1021/acs.jmedchem.2c00636
J. Med. Chem. XXXX, XXX, XXX−XXX

DMSO-d_6) δ 179.40, 169.75, 163.28, 158.91, 138.70, 133.54, 127.07, 126.66, 123.29, 121.31, 120.84, 113.36, 109.90, 24.00. HRMS (ESI-TOF) m/z for ($C_{14}H_{11}N_3OS$ [M + Na]$^+$) calcd 292.0521, found 292.0516. HPLC t_R = 6.635 min.

*S-(4,6-Dimethylpyrimidin-2-yl)-1H-indole-2-carbothioate (**3y**).* The product **3y** was synthesized from the reaction of indole-2-carboxylic acid (**1a**, 201 mg, 1.25 mmol) and 4,6-dimethylpyrimidine-2-thiol (**2m**, 175 mg, 1.25 mmol) in the presence of pyridine (0.110 mL, 1.1 equiv; 0.161 mL, 1.6 equiv). Yellow solid; yield 70% (248 mg); Mp: 142−144 °C. ^{1}H NMR (400 MHz, DMSO-d_6) δ 12.19 (s, 1H), 7.85 (d, J = 6.6 Hz, 1H), 7.57 (s, 2H), 7.44 (s, 2H), 7.23 (t, J = 12.9 Hz, 1H), 2.55 (d, J = 19 .3 Hz, 6H). ^{13}C NMR (101 MHz, DMSO-d_6) δ 179.66, 168.89, 162.78, 138.63, 133.62, 127.07, 126.59, 123.26, 121.28, 120.10, 113.34, 109.71, 23.76. HRMS (ESI-TOF) m/z for ($C_{15}H_{13}N_3OS$ [M + Na]$^+$) calcd 306.0677, found 306.0671. HPLC t_R = 7.380 min.

*S-(4-Methylpyrimidin-2-yl)-6-ethoxy-1H-indole-2-carbothioate (**3z**).* The product **3z** was synthesized from the reaction of 6-ethoxy-1*H*-indole-2-carboxylic acid (**1m**, 256 mg, 1.25 mmol) and 4-methyl pyrimidine-2-thiol (**2l**, 157 mg, 1.25 mmol) in the presence of pyridine (0.110 mL, 1.1 equiv; 0.161 mL, 1.6 equiv). Yellow solid; yield 48% (187 mg); Mp: 177−179 °C. ^{1}H NMR (400 MHz, DMSO-d_6) δ 12.06 (s, 1H), 8.19 (d, J = 5.8 Hz, 1H), 7.61 (d, J = 8.9 Hz, 1H), 7.44 (d, J = 1.4 Hz, 1H), 6.89 (d, J = 2.1 Hz, 1H), 6.86 (d, J = 5.8 Hz, 1H), 6.80 (dd, J = 8.8, 2.2 Hz, 1H), 4.08 (q, J = 6.9 Hz, 2H), 2.56 (s, 3H), 1.48−1.33 (m, 3H). ^{13}CNMR (101 MHz, DMSO-d_6) δ 187.90, 168.47, 167.46, 158.24, 157.93, 156.89, 140.01, 124.17, 123.64, 121.06, 118.52, 113.26, 112.44, 94.33, 63.20, 23.52, 14.61. HRMS (ESI-TOF) m/z for ($C_{16}H_{15}N_3O_2S$ [M + Na]$^+$) calcd 336.0783, found 336.0770. HPLC t_R = 9.958 min.

*S-(Pyrimidin-2-yl)-5-phenylfuran-2-carbothioate (**3aa**).* The product **3aa** was synthesized from the reaction of 5-phenylfuran-2-carboxylic acid (**1i**, 235 mg, 1.25 mmol) and pyrimidine-2-thiol (**2k**, 140 mg, 1.25 mmol) in the presence of pyridine (0.110 mL, 1.1 equiv; 0.161 mL, 1.6 equiv). Yellow solid; yield 56% (198 mg); Mp: 135−137 °C. ^{1}H NMR (400 MHz, $CDCl_3$) δ 8.75 (d, J = 4.9 Hz, 2H), 7.88−7.63 (m, 2H), 7.42−7.35 (m, 2H), 7.35−7.29 (m, 2H), 7.23 (t, J = 4.9 Hz, 1H), 6.76 (d, J = 3.7 Hz, 1H). ^{13}C NMR (101 MHz, $CDCl_3$) δ 175.42, 164.78, 158.61, 158.42, 148.81, 129.58, 129.02, 128.98, 125.12, 120.06, 119.84, 107.77. HRMS (ESI-TOF) m/z for ($C_{15}H_{10}N_2O_2S$ [M + Na]$^+$) calcd 305.0361, found 305.03551. HPLC t_R = 7.375 min.

*S-(4,6-Dimethylpyrimidin-2-yl)-5-(phenylethynyl)furan-2-carbothioate (**3ab**).* The product **3ab** was synthesized from the reaction of 5-(phenylethynyl)furan-2-carboxylic acid (**1j**, 265 mg, 1.25 mmol) and 4,6-dimethylpyrimidine-2-thiol (**2m**, 175 mg, 1.25 mmol) in the presence of pyridine (0.110 mL, 1.1 equiv; 0.161 mL, 1.6 equiv). Light brown solid; yield 63% (263 mg); Mp: 109−111 °C. ^{1}H NMR (400 MHz, DMSO-d_6) δ 7.67 (dd, J = 7.9, 1.6 Hz, 2H), 7.64 (d, J = 3.8 Hz, 1H), 7.57−7.46 (m, 3H), 7.36 (s, 1H), 7.22 (d, J = 3.8 Hz, 1H), 2.47 (s, 6H). ^{13}C NMR (101 MHz, DMSO-d_6) δ 175.94, 169.10, 161.81, 149.49, 140.34, 132.15, 130.74, 129.50, 120.55, 120.42, 119.81, 119.04, 96.46, 78.78, 23.85, 23.73. HRMS (ESI-TOF) m/z for ($C_{19}H_{14}N_2O_2S$ [M + Na]$^+$) calcd 357.0674, found 357.0665. HPLC t_R = 8.775 min.

*S-(Pyrimidin-2-yl)-benzo[b]thiophene-2-carbothioate (**3ac**).* The product **3ac** was synthesized from the reaction of benzo[*b*]thiophene-2-carboxylic acid (**1n**, 222 mg, 1.25 mmol) and pyrimidine-2-thiol (**2k**, 140 mg, 1.25 mmol) in the presence of pyridine (0.110 mL, 1.1 equiv; 0.161 mL, 1.6 equiv). Yellow crystalline solid; yield 69% (235 mg); Mp: 105−107 °C. ^{1}H NMR (400 MHz, DMSO-d_6) δ 8.95 (t, J = 5.6 Hz, 2H), 8.54 (s, 1H), 8.13 (d, J = 8.2 Hz, 2H), 7.77−7.34 (m, 3H). ^{13}C NMR (101 MHz, DMSO-d_6) δ 181.54, 163.50, 159.71, 142.01, 139.93, 138.94, 131.37, 128.86, 127.20, 126.19, 123.73, 121.75. HRMS (ESI-TOF) m/z for ($C_{13}H_8N_2OS_2$ [M + Na]$^+$) calcd 294.9976, found 294.9972. HPLC t_R = 8.018 min.

*S-(Pyrimidin-2-yl)-5-phenylthiophene-2-carbothioate (**3ad**).* The product **3ad** was synthesized from the reaction of 5-phenylthiophene-2-carboxylic acid (**1o**, 306 mg, 1.25 mmol) and pyrimidine-2-thiol (**2k**, 140 mg, 1.25 mmol) in the presence of pyridine (0.110 mL, 1.1 equiv; 0.161 mL, 1.6 equiv). Light yellow solid; yield 60% (223 mg); Mp: 118−120 °C. ^{1}H NMR (400 MHz, $CDCl_3$) δ 8.75 (d, J = 4.9 Hz, 2H), 7.82 (d, J = 4.1 Hz, 1H), 7.66−7.52 (m, 2H), 7.32 (dd, J = 4.9, 2.0 Hz, 3H), 7.29 (t, J = 4.2 Hz, 1H), 7.24 (t, J = 4.9 Hz, 1H). ^{13}C NMR (101 MHz, $CDCl_3$) δ 179.11, 164.93, 158.48, 157.93, 153.66, 139.40, 133.63, 132.96, 129.38, 129.21, 126.40, 123.98, 120.12, 29.71. HRMS (ESI-TOF) m/z for ($C_{15}H_{10}N_2OS_2$ [M + Na]$^+$) calcd 321.0133, found 321,0127. HPLC t_R = 8.095 min.

*S-(Pyrimidin-2-yl)-5-(4-bromophenyl)thiophene-2-carbothioate (**3ae**).* The product **3ae** was synthesized from the reaction of 5-(4-bromophenyl)thiophene-2-carboxylic acid (**1p**, 354 mg, 1.25 mmol) and pyrimidine-2-thiol (**2k**, 140 mg, 1.25 mmol) in the presence of pyridine (0.110 mL, 1.1 equiv; 0.161 mL, 1.6 equiv). Light yellow solid; yield 58% (274 mg); Mp: 137−139 °C. ^{1}H NMR (400 MHz, $CDCl_3$) δ 8.76 (d, J = 4.9 Hz, 2H), 7.80 (s, 1H), 7.56−7.39 (m, 4H), 7.26 (dd, J = 9.5, 4.5 Hz, 2H). ^{13}C NMR (101 MHz, $CDCl_3$) δ 179.12, 164.80, 158.50, 152.03, 139.85, 133.54, 132.53, 132.38, 131.93, 127.81, 124.28, 123.53, 120.16. HRMS (ESI-TOF) m/z for ($C_{15}H_9BrN_2OS_2$ [M + Na]$^+$) calcd 398.9238, found 398.9234. HPLC t_R = 8.571 min.

*S-(Pyrimidin-2-yl)quinoline-2-carbothioate (**3af**).* The product **3af** was synthesized from the reaction of quinoline-2-carboxylic acid (**1q**, 216 mg, 1.25 mmol) and pyrimidine-2-thiol (**2k**, 140 mg, 1.25 mmol) in the presence of pyridine (0.110 mL, 1.1 equiv; 0.161 mL, 1.6 equiv). Brown solid; yield 67% (224 mg); Mp: 142−144 °C. ^{1}H NMR (400 MHz, $CDCl_3$) δ 8.80 (d, J = 4.9 Hz, 2H), 8.23 (dd, J = 10.7, 8.7 Hz, 2H), 7.97 (d, J = 8.4 Hz, 1H), 7.83 (d, J = 8.2 Hz, 1H), 7.76 (ddd, J = 8.4, 6.9, 1.4 Hz, 1H), 7.62 (ddd, J = 8.1, 7.0, 1.1 Hz, 1H), 7.26 (t, J = 4.9 Hz, 1H). ^{13}C NMR (101 MHz, $CDCl_3$) δ 191.16, 166.22, 158.32, 150.71, 147.07, 137.61, 130.53, 130.47, 129.10, 127.75, 120.00, 117.11. HRMS (ESI-TOF) m/z for ($C_{14}H_9N_3OS$ [M + Na]$^+$) calcd 290.0364, found 290.0360. HPLC t_R = 8.329 min.

*S-(Pyrimidin-2-yl)-(S)-2-(6-methoxynaphthalen-2-yl)-propanethioate (**3ag**).* The product **3ag** was synthesized from the reaction of (*S*)-2-(6-methoxynaphthalen-2-yl)propanoic acid (**1r**, 287 mg, 1.25 mmol) and pyrimidine-2-thiol (**2k**, 140 mg, 1.25 mmol) in the presence of pyridine (0.110 mL, 1.1 equiv; 0.161 mL, 1.6 equiv). Brown solid; yield 71% (287 mg); Mp: 164−166 °C. ^{1}H NMR (400 MHz, $CDCl_3$) δ 8.69 (d, J = 4.9 Hz, 2H), 7.66 (dd, J = 8.8, 3.9 Hz, 3H), 7.37 (dd, J = 8.5, 1.8 Hz, 1H), 7.16 (d, J = 4.9 Hz, 1H), 7.16−6.95 (m, 2H), 4.10 (q, J = 7.1 Hz, 1H), 3.85 (s, 3H), 1.62 (d, J = 7.1 Hz, 3H). ^{13}C NMR (101 MHz, $CDCl_3$) δ 197.13, 165.16, 158.31, 157.92, 134.16, 133.72, 129.45, 128.97, 127.54, 127.39, 126.56, 119.96, 119.17, 105.63, 55.34, 54.94, 18.29. HRMS (ESI-TOF) m/z for ($C_{18}H_{16}N_2O_2S$ [M + Na]$^+$) calcd 347.0830, found 347.0826. HPLC t_R = 9.212 min.

*S-(Benzo[d]thiazol-2-yl)-1H-indole-2-carbothioate (**3ah**).* The product **3ah** was synthesized from the reaction of indole-2-carboxylic acid (**1a**, 201 mg, 1.25 mmol) and benzo[*d*]thiazole-2-thiol (**2n**, 209 mg, 1.25 mmol) in the presence of pyridine (0.110 mL, 1.1 equiv; 0.161 mL, 1.6 equiv). Light yellow solid; yield 73% (283 mg); Mp: 215−217 °C. ^{1}H NMR (400 MHz, DMSO-d_6) δ 12.39 (s, 1H), 8.23 (dd, J = 7.9, 0.7 Hz, 1H), 8.07 (d, J = 7.5 Hz, 1H), 7.79 (d, J = 8.1 Hz, 1H), 7.68 (s, 1H), 7.59 (dd, J = 9.4, 7.6 Hz, 1H), 7.52 (dd, J = 6.3, 4.7 Hz, 2H), 7.39 (dd, J = 8.3, 6.9 Hz, 1H), 7.27−7.11 (m, 1H). ^{13}C NMR (101 MHz, DMSO-d_6) δ 177.79, 157.68, 151.58, 139.03, 135.99, 132.25, 127.32, 127.19, 127.14, 126.26, 123.49, 122.98, 122.55, 121.63, 113.47, 111.00. HRMS (ESI-TOF) m/z for ($C_{16}H_{10}N_2OS_2$ [M + Na]$^+$) calcd 333.0133, found 333.0129. HPLC t_R = 10.675 min.

*S-(Benzo[d]thiazol-2-yl)benzofuran-2-carbothioate (**3ai**).* The product **3ai** was synthesized from the reaction of benzofuran-2-carboxylic acid (**1g**, 203 mg, 1.25 mmol) and benzo[*d*]thiazole-2-thiol (**2n**, 209 mg, 1.25 mmol) in the presence of pyridine (0.110 mL, 1.1 equiv; 0.161 mL, 1.6 equiv). Yellow solid; yield 79% (307 mg); Mp: 198−200 °C. ^{1}H NMR (400 MHz, $CDCl_3$) δ 8.01 (d, J = 8.2 Hz, 1H), 7.94−7.81 (m, 1H), 7.69 (d, J = 7.9 Hz, 1H), 7.64 (d, J = 0.8 Hz, 1H), 7.58 (dd, J = 8.5, 0.7 Hz, 1H), 7.51−7.42 (m, 2H), 7.42−7.34 (m, 1H), 7.34−7.25 (m, 1H). ^{13}C NMR (101 MHz, $CDCl_3$) δ 177.10, 156.62, 155.98, 151.71, 149.41, 136.20, 129.15, 126.77, 126.45, 125.72, 124.52, 123.57, 123.14, 121.27, 113.55, 112.67. HRMS (ESI-TOF) m/z for ($C_{16}H_9NOS_2$ [M + Na]$^+$) calcd 333.9973, found 333.9967. HPLC t_R = 9.522 min.

*S-(Benzo[d]thiazol-2-yl)-5-phenylfuran-2-carbothioate (**3aj**).* The product **3aj** was synthesized from the reaction of 5-phenylfuran-2-carboxylic acid (**1i**, 235 mg, 1.25 mmol) and benzo[*d*]thiazole-2-thiol

https://doi.org/10.1021/acs.jmedchem.2c00636
J. Med. Chem. XXXX, XXX, XXX−XXX

(**2n**, 209 mg, 1.25 mmol) in the presence of pyridine (0.110 mL, 1.1 equiv; 0.161 mL, 1.6 equiv). Light yellow solid; yield 59% (249 mg); Mp: 143−145 °C. ^{1}H NMR (400 MHz, DMSO-d_6) δ 8.23 (dd, J = 7.9, 0.8 Hz, 1H), 8.18−8.03 (m, 1H), 7.95 (dd, J = 5.3, 3.3 Hz, 2H), 7.89 (d, J = 3.9 Hz, 1H), 7.66−7.46 (m, 5H), 7.44 (d, J = 3.9 Hz, 1H). ^{13}C NMR (101 MHz, DMSO-d_6) δ 178.94, 168.13, 167.63, 159.62, 156.68, 154.38, 147.54, 144.48, 136.02, 129.57, 129.43, 127.41, 126.02, 125.48, 124.85, 122.86, 122.71, 120.34, 108.39. HRMS (ESI-TOF) m/z for ($C_{18}H_{11}NO_2S_2$ [M + Na]$^+$) calcd. 360.0128, found 360.0124. HPLC t_R = 9.856 min.

*S-(Benzo[d]thiazol-2-yl)-5-(4-bromophenyl)furan-2-carbothioate (**3ak**).* The product **3ak** was synthesized from the reaction of 5-(4-bromophenyl)furan-2-carboxylic acid (**1s**, 333 mg, 1.25 mmol) and benzo[d]thiazole-2-thiol (**2n**, 209 mg, 1.25 mmol) in the presence of pyridine (0.110 mL, 1.1 equiv; 0.161 mL, 1.6 equiv). Light yellow solid; yield 80% (416 mg); Mp: 206−208 °C. ^{1}H NMR (400 MHz, $CDCl_3$) δ 8.00 (d, J = 7.9 Hz, 1H), 7.88 (d, J = 7.7 Hz, 1H), 7.62 (d, J = 8.3 Hz, 2H), 7.54 (d, J = 8.3 Hz, 2H), 7.46 (dd, J = 14.0, 6.7 Hz, 1H), 7.38 (dd, J = 8.7, 5.6 Hz, 2H), 6.81 (d, J = 3.6 Hz, 1H). ^{13}C NMR (101 MHz, $CDCl_3$) δ 165.29, 158.45, 158.05, 134.29, 133.86, 129.59, 129.10, 127.67, 127.52, 126.69, 120.09, 119.30, 105.77, 55.48, 55.07, 18.43. HRMS (ESI-TOF) m/z for ($C_{18}H_{10}BrNO_2S_2$ [M + Na]$^+$) calcd. 437.9229, found 437. 9222. HPLC t_R = 7.519 min.

*S-(Benzo[d]thiazol-2-yl)benzo[b]thiophene-2-carbothioate (**3al**).* The product **3al** was synthesized from the reaction of benzo[b]-thiophene-2-carboxylic acid (**1n**, 222 mg, 1.25 mmol) and benzo[d]-thiazole-2-thiol (**2n**, 209 mg, 1.25 mmol) in the presence of pyridine (0.110 mL, 1.1 equiv; 0.161 mL, 1.6 equiv). Light yellow solid; yield 68% (278 mg); Mp: 197−199 °C. ^{1}H NMR (400 MHz, $CDCl_3$) δ 8.15 (s, 1H), 8.00 (d, J = 7.9 Hz, 1H), 7.89 (d, J = 8.0 Hz, 1H), 7.88−7.76 (m, 2H), 7.52−7.42 (m, 2H), 7.42−7.31 (m, 2H). ^{13}C NMR (101 MHz, $CDCl_3$) δ 180.14, 157.09, 151.92, 142.79, 139.57, 138.63, 136.45, 130.20, 128.37, 126.58, 126.47, 125.83, 125.73, 123.30, 123.12, 121.40. HRMS (ESI-TOF) m/z for ($C_{16}H_9NOS_3$ [M + Na]$^+$) calcd 349.9744, found 349.9739. HPLC t_R = 10.389 min.

*S-(Benzo[d]thiazol-2-yl)-5-phenylthiophene-2-carbothioate (**3am**).* The product **3al** was synthesized from the reaction of 5-phenylthiophene-2-carboxylic acid (**1o**, 306 mg, 1.25 mmol) and benzo[d]thiazole-2-thiol (**2n**, 209 mg, 1.25 mmol) in the presence of pyridine (0.110 mL, 1.1 equiv; 0.161 mL, 1.6 equiv). Light yellow solid; yield 62% (274 mg); Mp: 188−190 °C. ^{1}H NMR (400 MHz, $CDCl_3$) δ 7.99 (d, J = 8.0 Hz, 1H), 7.86 (t, J = 5.2 Hz, 2H), 7.61 (dd, J = 8.0, 1.4 Hz, 2H), 7.52−7.41 (m, 1H), 7.41−7.34 (m,3H), 7.36−7.28 (m, 2H). ^{13}C NMR (101 MHz, $CDCl_3$) δ 178.08, 157.50, 154.51, 151.67, 138.19, 136.22, 133.96, 132.73, 129.64, 129.29, 126.48, 126.38, 125.56, 124.23, 123.03, 121.23. HRMS (ESI-TOF) m/z for ($C_{18}H_{11}NOS_3$ [M + Na]$^+$) calcd 375.9901 found 375.9895. HPLC t_R = 10.973 min.

*S-(Benzo[d]thiazol-2-yl)quinoline-2-carbothioate (**3an**).* The product **3al** was synthesized from the reaction of quinoline-2-carboxylic acid (**1q**, 216 mg, 1.25 mmol) and benzo[d]thiazole-2-thiol (**2n**, 209 mg, 1.25 mmol) in the presence of pyridine (0.110 mL, 1.1 equiv; 0.161 mL, 1.6 equiv). Light yellow solid; yield 66% (340 mg); Mp: 182−184 °C. ^{1}H NMR (400 MHz, $CDCl_3$) δ 8.30 (d, J = 8.4 Hz, 1H), 8.22 (dd, J = 8.5, 3.6 Hz, 1H), 8.06−7.99 (m, 2H), 7.91−7.83 (m, 2H), 7.82−7.75 (m, 1H), 7.65 (dd, J = 8.1, 7.0 Hz, 1H), 7.49−7.41 (m, 1H), 7.38 (dd, J = 7.7, 1.2 Hz, 1H). ^{13}C NMR (101 MHz, $CDCl_3$) δ 190.16, 159.97, 152.17, 150.18, 147.18, 138.07, 136.32, 130.64, 129.62, 127.97, 126.42, 125.61, 123.21, 121.40, 117.20. HRMS (ESI-TOF) m/z for ($C_{17}H_{10}N_2OS_2$ [M + Na]$^+$) calcd 345.0133, found 345.0127. HPLC t_R = 10.031 min.

Computational Analyses. *Library Preparation and Virtual Screening.* We did this by virtually screening our in-house TüKIC library against the M^{pro} using a combination of docking and short MD simulations. Three-dimensional ligand structures were generated with LigPrep (implemented in Maestro 2020v4), using Epik to predict their protonation in pH 7.0 ± 2.0 and generating tautomers and diastereoisomers. The OPLS3e force-field was employed for structure generation.

The SARS-CoV-2 M^{pro} protein structure was previously prepared from the PDB ID: 5R82[40,56] using the Protein Wizard Preparation tool, with standard options, and MD simulations for equilibration as described. Molecular docking was carried out with Glide SP (version 9.1).[57] Grids were centered at the central point of the active site residues G143, C145, M49, and H41. The box was 12 Å long in each direction. The top 500 hits were visually inspected by observing the interaction with relevant residues within P1 and P2. Whenever mentioned, covalent docking as performed using CovDock[58] using the C145 as the anchor and nucleophilic addition to the double bond as the reaction type and generating up to 10 poses for each ligand. Poses were selected according to the docking score and relevant interactions. Selected poses underwent short MD simulations (200 ns, data not shown). Ligands that remained within the pocket during the simulated time were further selected for experimental testing.

Potential Binding Mode of Compounds in MERS-CoV and SARS-CoV-1 Main Proteases. The ligands **3w** and **3af** were covalently docked to the MERS and SARS-CoV-1 M^{pro} models to study their binding mode. 3D structural models M^{pro} from MERS (PDB ID: 4YLU), SARS-Cov-1 (7LMJ), and SARS-CoV-2 were generated, filling the missing residues in the C-terminal portion, using Prime.[59,60] The generated models then underwent preparation using PrepWizard (Maestro 2021.4).

MD Simulations and Trajectory Analyses. The minimized structures were submitted to MD simulation for further refinement. Selected docking poses were further validated by MD simulation, where ligand stability within the proposed pocket and its interactions were evaluated. MD simulations were carried out using the Desmond engine[61] with the OPLS4 force-field.[62] The simulated system encompassed the protein−ligand complex, a predefined water model (TIP3P)[63] as a solvent, and counterions (Na^+ or Cl^- adjusted to neutralize the overall system charge). The system was treated in a cubic box with periodic boundary conditions specifying the shape and the size of the box as 13 Å distance from the box edges to any atom of the protein. RESPA integrator time steps of 2 fs for bonded and near and 6 fs for far were applied. Short-range Coulombic interactions were performed using a time step of 1 fs and a cutoff value of 9.0 Å, whereas long-range Coulombic interactions were handled using the Smooth Particle Mesh Ewald (PME) method.[64]

Desmond Relaxation Protocol. Simulations were run in NPT ensemble, with a temperature of 310 K (Nosé−Hoover thermostat) and pressure of 1.01325 bar (Martyna−Tobias−Klein barostat).

Results of simulations, in the form of trajectory and interaction data and RMSD and RMSF values, are available on the Zenodo repository (code: 10.5281/zenodo.6303511). MD trajectories were visualized, and figures were produced using PyMOl v.2.5 (Schrödinger LCC, New York, NY, USA). For each ligand, simulations at least five independent 200 ns replicas were carried out. Protein−ligand interactions were determined using the Simulation Event Analysis pipeline implemented in Maestro (Maestro v2021.4) with standard settings.

SARS-CoV-2 M^{pro} Assay. The SARS-CoV-2 main protease (M^{pro}) was expressed and purified according to a previously published procedure.[37] In brief, a codon-optimized cDNA sequence encoding the M^{pro} enzyme (accession no.: MN908947.3, ORF1ab polyprotein residues 3264−3569) with an N-terminal M^{pro} autocleavage site and a C-terminal His_{10} tag linked via an HRV 3C protease cleavage site was inserted into the bacterial expression vector pGEX-6P-1. After transformation of BL21 *Escherichia coli* bacteria (NEB, Ipswich, USA), cells were grown in an LB medium supplemented with ampicillin (100 μg/mL). Subsequently, IPTG (final concentration 1 mM) was added to induce recombinant gene expression until an OD_{600} of 0.5 was reached. After growing the bacteria at 30 °C for 3−4 h, cells were sedimented at 4000g and 4 °C for 10 min. Cells were then resuspended in cold PBS supplemented with 5 mM imidazole (pH 7.4). Subsequently, the cells were lyzed on ice using a Sonoplus HD2070 (Bandelin, Berlin, Germany) and centrifuged at 48,000g and 4 °C for 30 min in collect the supernatant. The His-tagged M^{pro} enzyme was purified using HisPur Ni-NTA spin columns (Thermo Fisher Scientific, Waltham, USA). For the native M^{pro} enzyme, the His tag was removed by an HRV 3C protease (Merck, Darmstadt, Germany) overnight at 4 °C. Subsequent disposal of the GST-tagged HRV 3C protease was performed by a Glutathione Spin Column (Thermo Fisher Scientific,

https://doi.org/10.1021/acs.jmedchem.2c00636
J. Med. Chem. XXXX, XXX, XXX−XXX

Waltham, USA). The collected flow through contained the native M^{pro} enzyme that was subsequently used for pharmacological assays. For the initial inhibition experiments at a single concentration, crude cell extracts containing the M^{pro} enzyme were used. For the subsequent pharmacological characterization of hit compounds to determine IC_{50}, K_i, and k_{inac}/K_i values, we employed the purified His-tagged M^{pro}.

SARS-CoV-2 M^{pro} activity assays were performed as previously established.[37] Frozen recombinant His-tagged SARS-CoV-2 M^{pro} was thawed and immediately used for the enzyme assays that were performed on a Pherastar FSX plate reader (BMG Labtech, Offenburg, Germany) at 37 °C with an excitation wavelength of 360 nm and an emission wavelength of 460 nm. Black half area 96-well plates with a flat bottom were obtained from Greiner Bio-One (Kremsmünster, Austria). The assay buffer contained 50 mM 3-(*N*-morpholino)propanesulfonic acid (MOPS, pH 7.2), 10 mM NaCl, 1 mM EDTA, and 0.01% Triton X-100. The fluorogenic substrate Boc-Abu-Tle-Leu-Gln-AMC[37] diluted in the assay buffer was added to the test compounds, and the mixture was preincubated at 37 °C for 5 min. The proteolytic cleavage of the substrate was started by addition of the enzyme (e.g., 400 ng His-tagged M^{pro} diluted in the assay buffer), and the fluorescence increase was followed for 10 or 60 min, respectively. The final protein concentration of SARS-CoV-2 M^{pro} was adjusted to a slope increase of approximately 2000/min within the initial 10 min. The final substrate concentration was 50 μM, which approximately corresponds to its K_m value.[37] The final DMSO concentration was 4%. The product formation rate of the uninhibited control was set at 100%. For the determination of concentration−inhibition curves, at least eight different inhibitor concentrations were investigated to observe the respective product formation rates during the first 10 min. IC_{50} values were calculated by nonlinear regression. For inhibitors showing time-dependent inhibition, the second-order rate constant k_{inac}/K_i was determined by monitoring the effects of five different inhibitor concentrations on the product formation rate for 60 min, and the data were analyzed by nonlinear regression using the equation $[P] = (v_i \times (1 - \exp(-k_{obs} \times t)/k_{obs} + d))$, where $[P]$ is the product concentration, v_i is the initial rate, k_{obs} is the observed first-order rate constant, and d is the offset. Subsequently, k_{obs} was plotted versus the inhibitor concentration $[I]$, and a nonlinear regression using the equation $k_{obs} = (k_{inac} \times [I])/([I] + K_i \times (1 + [S]/K_m))$ was performed. The deviation of each data point from the calculated nonlinear regression was less than 10%. Data were analyzed using GraphPad Prism 8.0.

Assay against Recombinant SARS-CoV-1 M^{pro} and MERS-CoV M^{pro}. Recombinant SARS-CoV-1 Mpro and MERS-CoV Mpro were purchased from R&D Systems. Proteolytic activity was determined using 10 μM MCA-AVLQSGFR-K(DNP)-K-NH_2 for SARS-CoV-1 Mpro and 10 μM Ac-Abu-Tle-Leu-Gln-ACC for MERS-CoV Mpro. Fluorescence was monitored in a Synergy HTX (Biotek) plate reader using excitation/emission wavelengths of 320/400 nm for MCA-AVLQSGFR-K(DNP)-K-NH_2 and 360/460 nm for Ac-Abu-Tle-Leu-Gln-ACC. All assays were performed in 384-well black plates with a 15 min preincubation of the compounds with the enzyme. The screen was performed with 10 μM of inhibitors. Compounds that inhibited enzyme activity by 50% or more in the initial screen had their dose−response curve determined. For each compound, two independent experiments were performed, each in triplicate and monitored for 2 h. The percentage of inhibition was calculated by comparison to a DMSO control. The protease inhibitor GC373 was used as a positive control. Assays were performed at 25 °C in a final volume of 30 μL per well of 50 mM HEPES (pH 7.5), 150 mM sodium chloride, 1 mM EDTA, and 0.01% Tween 20 in the presence of 50 nM enzyme and 10 μM substrate.[51,52,65] The half-maximal inhibitory concentration (IC_{50}) was determined by nonlinear regression analysis of the velocity vs inhibitor concentration plot using GraphPad Prism 6.[66] Eleven inhibitor concentrations were used to generate each curve.

Cytotoxicity. *Cell Cultures.* Calu-3 cells (human lung, ATCC Cat# HTB-55) were maintained in Dulbecco's modified Eagle medium (DMEM)/F-12 supplemented with 10% FCS and 10 mM sodium pyruvate. Vero E6 cells (African green monkey kidney, ATCC cat. #CRL-1586) were maintained in DMEM supplemented with 5% FCS. All cell lines were incubated at 37 °C and 5% CO_2 in a humidified atmosphere.

Cell Vitality Assay. To determine cell vitality of Calu-3 cells treated with inhibitors, the CellTiter-Glo Luminescent Cell Viability Assay Kit (Promega) was used. Cells were grown in 96-well plates until reaching 50−60% confluency before they were incubated with DMSO (solvent control) or M^{pro} inhibitors at a concentration of 10 μM for 24 h. Next, cell culture supernatants were removed, and 50 μL of the CellTiter-Glo substrate was added to each well and incubated for 30 min on a rocking platform. Finally, samples were transferred into white 96-well plates, and luminescence was measured using a Hidex Sense plate luminometer (Hidex).

Antiviral Activity. All work with infectious SARS-CoV-2 was conducted under BSL-3 conditions at the German Primate Centre, Göttingen/Germany. Calu-3 cells were grown in 48-well plates until reaching approx. 70% confluency. Cells were incubated with 10-fold serial dilutions (10−0.001 μM) of M^{pro} inhibitors for 1 h at 37 °C prior infection. Next, the inhibitor containing the cell culture medium was removed, and cells were infected with SARS-CoV-2 isolate NK, Pango lineage B.1.513, at an MOI of 0.01 in an inoculum volume of 400 μL for 1 h at 37 °C. At 1 h post infection (p.i.), the inoculum was removed, and cells were washed with PBS three times and further incubated in a cell culture medium containing the respective inhibitor for 24 h. Virus-containing supernatants were harvested and stored at −80 °C until further usage.

To determine viral titers, confluent grown Vero E6 cells were inoculated for 1 h at 37 °C with 10-fold serial dilutions of virus-containing supernatants. Next, the inoculum was removed, and cells were washed once with PBS before they were overlaid with 1% plaque agarose (Biozym) dissolved in Eagle's minimal essential medium without phenol red (Lonza) and further incubated. At 48 h p.i., virus-induced plaques were counted, and viral titers were determined as plaque forming units (PFU)/mL.

Crystallography Procedure. The cDNA of SARS-CoV-2 M^{pro} (GenBank: MN908947.3) with the N-terminal SUMO tag was cloned into the pET-15b vector. The plasmid was transformed into BL21 (DE3) cells for protein expression. The expressed protein was purified by a Ni-NTA column (GE Healthcare) and cleaved by the SUMO specific peptidase 2 (SENP2) to remove the SUMO tag. The resulting protein sample was further purified by Q-Sepharose followed by a size-exclusion chromatography (GE Healthcare). The eluted protein samples were stored in a solution (10 mM Tris, pH 7.5).

The purified protease was concentrated to 7 mg/mL for crystallization. To obtain complex structures, the protein was incubated with 4 mM **3w** and **3af** for 1 h before crystallization condition screening. Crystals of the complexes were obtained under the condition of 10−22% PEG6000, 100 mM MES, pH 5.75−6.25, and 3% DMSO. Crystals were flash frozen in liquid nitrogen in the presence of the reservoir solution supplemented with 20% glycerol. X-ray diffraction data were collected at beamline BL02U1 at the Shanghai Synchrotron Radiation Facility.[67] The data were processed with HKL3000 software packages.[68] The complex structures were solved by molecular replacement using the program PHASER[69] with a search model of PDB code 6M2N.[67] The model was built using Coot[68] and refined with XYZ (reciprocal-space), individual B factors, TLS parameters, and occupancies implemented in the program PHENIX.[69] The refined structures were deposited to the Protein Data Bank with accession codes listed in Table S2 in the Supporting Information. The complete statistics as well as the quality of the solved structures are also shown in Table S2.

Glutathione (GSH) Stability Assay. The GSH stability assay for compounds was performed according to the reported procedures.[70,71] A suitable HPLC/MS method was prepared, and the HPLC method was adjusted to inject a sample every 10 min. To achieve a final concentration of 10 μM inhibitor and 5 mM GSH in a final volume of 1 mL, 1 μL of the inhibitor stock solution (10 mM) was added to 949 μL of the phosphate buffer (pH 7.4) as well as 50 μL of the stock solution (100 mM) GSH. The solution was directly pipetted into a HPLC vial and vortexed thoroughly. The temperature of the autosampler was set to 30 °C. Ten to 30 repeated measurements were performed. The

https://doi.org/10.1021/acs.jmedchem.2c00636
J. Med. Chem. XXXX, XXX, XXX−XXX

reaction of the inhibitor with GSH was monitored by measuring the decreasing area under the curve (AUC) of each compound.

■ ASSOCIATED CONTENT

Supporting Information

The Supporting Information is available free of charge at https://pubs.acs.org/doi/10.1021/acs.jmedchem.2c00636.

Inhibition of proteases (Figures S1−S7); cell vitality and antiviral activity of inhibitors (Figures S8−S12); broad-spectrum M^{pro} inhibitory activities of thioesters (Figures S13−S14); potential binding mode of compounds (Figure S15); GSH stability data for **3an** (Figure S16); selected hits from the virtual screening (Table S1); crystallography data collection and refinement statistics (Table S2); synthesis of LN5535 (Scheme S1); ^{1}H and ^{13}C NMR spectra and the HPLC traces of selected compounds; Preliminary Full wwPDB X-ray Structure Validation Report for**3w** and **3af** (PDF)

Molecular formula strings and the associated biological data (CSV)

3CLpro-3af (PDB code 7X6J) (PDB)

3CLpro-3w (PDB code 7X6K) (PDB)

CCDC file for **3w** (PDF)

CCDC file for **3af** (PDF)

Accession Codes

The authors will release the atomic coordinates (**3w,** PDB ID: 7X6K) (A) and (**3af,** PDBID: 7X6J) upon article publication.

■ AUTHOR INFORMATION

Corresponding Authors

Thanigaimalai Pillaiyar − *Institute of Pharmacy, Pharmaceutical/Medicinal Chemistry and Tübingen Center for Academic Drug Discovery, Eberhard Karls University Tübingen, Auf der Morgenstelle 8, 72076 Tübingen, Germany. Cluster of Excellence iFIT (EXC 2180) "Image-Guided & Functionally Instructed Tumor Therapies", University of Tübingen, Tübingen 72076, Germany;* orcid.org/0000-0001-5575-8896; Email: thanigaimalai.pillaiyar@uni-tuebingen.de

Yechun Xu − *CAS Key Laboratory of Receptor Research, and Stake Key Laboratory of Drug Research, Shanghai Institute of Materia Medica, Chinese Academy of Sciences, Shanghai 201203, China;* orcid.org/0000-0002-1581-6155; Email: ycxu@simm.ac.cn

Authors

Philipp Flury − *Institute of Pharmacy, Pharmaceutical/Medicinal Chemistry and Tübingen Center for Academic Drug Discovery, Eberhard Karls University Tübingen, Auf der Morgenstelle 8, 72076 Tübingen, Germany. Cluster of Excellence iFIT (EXC 2180) "Image-Guided & Functionally Instructed Tumor Therapies", University of Tübingen, Tübingen 72076, Germany*

Nadine Krüger − *Infection Biology Unit, German Primate Center, Leibniz Institute for Primate Research Göttingen, Göttingen 37077, Germany*

Haixia Su − *CAS Key Laboratory of Receptor Research, and Stake Key Laboratory of Drug Research, Shanghai Institute of Materia Medica, Chinese Academy of Sciences, Shanghai 201203, China*

Laura Schäkel − *PharmaCenter Bonn, Pharmaceutical Institute, Pharmaceutical & Medicinal Chemistry, University of Bonn, Bonn D-53121, Germany*

Elany Barbosa Da Silva − *Skaggs School of Pharmacy and Pharmaceutical Sciences, University of California San Diego, La Jolla, California 92093, United States;* orcid.org/0000-0002-1926-3500

Olga Eppler − *Institute of Pharmacy, Pharmaceutical/Medicinal Chemistry and Tübingen Center for Academic Drug Discovery, Eberhard Karls University Tübingen, Auf der Morgenstelle 8, 72076 Tübingen, Germany. Cluster of Excellence iFIT (EXC 2180) "Image-Guided & Functionally Instructed Tumor Therapies", University of Tübingen, Tübingen 72076, Germany*

Thales Kronenberger − *Institute of Pharmacy, Pharmaceutical/Medicinal Chemistry and Tübingen Center for Academic Drug Discovery, Eberhard Karls University Tübingen, Auf der Morgenstelle 8, 72076 Tübingen, Germany. Cluster of Excellence iFIT (EXC 2180) "Image-Guided & Functionally Instructed Tumor Therapies", University of Tübingen, Tübingen 72076, Germany*

Tianqing Nie − *CAS Key Laboratory of Receptor Research, and Stake Key Laboratory of Drug Research, Shanghai Institute of Materia Medica, Chinese Academy of Sciences, Shanghai 201203, China*

Stephanie Luedtke − *Skaggs School of Pharmacy and Pharmaceutical Sciences, University of California San Diego, La Jolla, California 92093, United States*

Cheila Rocha − *Infection Biology Unit, German Primate Center, Leibniz Institute for Primate Research Göttingen, Göttingen 37077, Germany*

Katharina Sylvester − *PharmaCenter Bonn, Pharmaceutical Institute, Pharmaceutical & Medicinal Chemistry, University of Bonn, Bonn D-53121, Germany*

Marvin R.I. Petry − *PharmaCenter Bonn, Pharmaceutical Institute, Pharmaceutical & Medicinal Chemistry, University of Bonn, Bonn D-53121, Germany*

James H. McKerrow − *Skaggs School of Pharmacy and Pharmaceutical Sciences, University of California San Diego, La Jolla, California 92093, United States;* orcid.org/0000-0002-5152-4627

Antti Poso − *Institute of Pharmacy, Pharmaceutical/Medicinal Chemistry and Tübingen Center for Academic Drug Discovery, Eberhard Karls University Tübingen, Auf der Morgenstelle 8, 72076 Tübingen, Germany. Cluster of Excellence iFIT (EXC 2180) "Image-Guided & Functionally Instructed Tumor Therapies", University of Tübingen, Tübingen 72076, Germany; School of Pharmacy, Faculty of Health Sciences, University of Eastern Finland, Kuopio 70211, Finland;* orcid.org/0000-0003-4196-4204

Stefan Pöhlmann − *Infection Biology Unit, German Primate Center, Leibniz Institute for Primate Research Göttingen, Göttingen 37077, Germany; Faculty of Biology and Psychology, University Göttingen, Göttingen 37073, Germany*

Michael Gütschow − *PharmaCenter Bonn, Pharmaceutical Institute, Pharmaceutical & Medicinal Chemistry, University of Bonn, Bonn D-53121, Germany;* orcid.org/0000-0002-9376-7897

Anthony J. O'Donoghue − *Skaggs School of Pharmacy and Pharmaceutical Sciences, University of California San Diego, La Jolla, California 92093, United States*

Christa E. Müller − *PharmaCenter Bonn, Pharmaceutical Institute, Pharmaceutical & Medicinal Chemistry, University*

of Bonn, Bonn D-53121, Germany; orcid.org/0000-0002-0013-6624

Stefan A. Laufer − *Institute of Pharmacy, Pharmaceutical/Medicinal Chemistry and Tübingen Center for Academic Drug Discovery, Eberhard Karls University Tübingen, Auf der Morgenstelle 8, 72076 Tübingen, Germany. Cluster of Excellence iFIT (EXC 2180) "Image-Guided & Functionally Instructed Tumor Therapies", University of Tübingen, Tübingen 72076, Germany;* orcid.org/0000-0001-6952-1486

Complete contact information is available at: https://pubs.acs.org/10.1021/acs.jmedchem.2c00636

Author Contributions

○These authors contributed equally.

Notes

The authors declare no competing financial interest.

■ ACKNOWLEDGMENTS

TüCAD2 is funded by the Federal Ministry of Education and Research (BMBF) and the Baden-Württemberg Ministry of Science as part of the Excellence Strategy of the German Federal and State Governments. N.K. thanks Stephan Ludwig, Institute of Virology, University of Münster, for providing Calu-3 cells and SARS-CoV-2 isolate. N.K. thanks Marcel Müller, Charité-Universitätsmedizin Berlin, for providing Vero E6 cells. T.K. is funded by the fortune initiative and from TüCAD2. The authors thank Lan Phuong Vu for synthesizing the M^{pro} substrate. The authors would like to thank CSC-Finland for the generous computational resources. Y.X. thanks funding by the Science and Technology Commission of Shanghai Municipality (No. 20430780300) and the staff from BL02U1 and BL18U1 beamline at Shanghai Synchrotron Radiation Facility for assistance during data collection. C.E.M., M.G., L.S., K.S., and M.R.I.P. were supported by the Volkswagen Foundation. The authors thank Kristine Schmidt for proofreading (language).

■ ABBREVIATIONS

ACE2, angiotensin-converting enzyme 2; ATP, adenosine triphosphate; CoV, coronavirus; COVID-19, coronavirus disease 19; DMSO, dimethyl sulfoxide; M^{pro}, SARS-CoV-2 main protease; Calu-3 cells, cultured human airway epithelial cells; DCM, dichloromethane; GSH, glutathione; HRMS, high-resolution mass spectrometry; HPLC, high-performance liquid chromatography; JAK, Janus kinase; MERS-CoV, Middle East respiratory syndrome; MDS, molecular dynamics simulation; MOI, multiplicity of infection; NSP, nonstructural protein; NMR, nuclear magnetic resonance; Pak, p21-activated kinase; PDB, Protein Data Bank; PDK-1, 3-phosphoinositide-dependent protein kinase-1; PL^{pro}, SARS-CoV-2 papain-like protease; P.I., post-infection; RNA, ribonucleic acid; RdRp, RNA-dependent RNA polymerase; SARS, severe acute respiratory syndrome; TLC, thin layer chromatography; TüKIC, Tübingen kinase inhibitor collection; TMPRSS2, transmembrane protease serine 2; Vero 76, Vero 76 clone E6 cells

■ REFERENCES

(1) Li, Q.; Guan, X.; Wu, P.; Wang, X.; Zhou, L.; Tong, Y.; Ren, R.; Leung, K. S. M.; Lau, E. H. Y.; Wong, J. Y.; Xing, X.; Xiang, N.; Wu, Y.; Li, C.; Chen, Q.; Li, D.; Liu, T.; Zhao, J.; Liu, M.; Tu, W.; Chen, C.; Jin, L.; Yang, R.; Wang, Q.; Zhou, S.; Wang, R.; Liu, H.; Luo, Y.; Liu, Y.; Shao, G.; Li, H.; Tao, Z.; Yang, Y.; Deng, Z.; Liu, B.; Ma, Z.; Zhang, Y.; Shi, G.; Lam, T. T. Y.; Wu, J. T.; Gao, G. F.; Cowling, B. J.; Yang, B.; Leung, G. M.; Feng, Z. Early transmission dynamics in Wuhan, China, of novel Coronavirus-infected pneumonia. *N. Engl. J. Med.* **2020**, *382*, 1199−1207.

(2) Zhou, P.; Yang, X. L.; Wang, X. G.; Hu, B.; Zhang, L.; Zhang, W.; Si, H. R.; Zhu, Y.; Li, B.; Huang, C. L.; Chen, H. D.; Chen, J.; Luo, Y.; Guo, H.; Jiang, R. D.; Liu, M. Q.; Chen, Y.; Shen, X. R.; Wang, X.; Zheng, X. S.; Zhao, K.; Chen, Q. J.; Deng, F.; Liu, L. L.; Yan, B.; Zhan, F. X.; Wang, Y. Y.; Xiao, G. F.; Shi, Z. L. A pneumonia outbreak associated with a new coronavirus of probable bat origin. *Nature* **2020**, *579*, 270−273.

(3) Fauci, A. S.; Lane, H. C.; Redfield, R. R. Covid-19 − Navigating the uncharted. *New. Engl. J. Med.* **2020**, *382*, 1268−1269.

(4) Mitsuya, H.; Kokudo, N. Sustaining containment of COVID-19: Global sharing for pandemic response. *Global Health Med.* **2020**, *2*, 53−55.

(5) *World Health Organization*; https://www.who.int/emergencies/diseases/novel-coronavirus-2019 (accessed 25 February-2022).

(6) Badua, C. L. D. C.; Baldo, K. A. T.; Medina, P. M. B. Genomic and proteomic mutation landscapes of SARS-CoV-2. *J. Med. Virol.* **2021**, *93*, 1702−1721.

(7) Lopez Bernal, J.; Andrews, N.; Gower, C.; Gallagher, E.; Simmons, R.; Thelwall, S.; Stowe, J.; Tessier, E.; Groves, N.; Dabrera, G.; Myers, R.; Campbell, C. N. J.; Amirthalingam, G.; Edmunds, M.; Zambon, M.; Brown, K. E.; Hopkins, S.; Chand, M.; Ramsay, M. Effectiveness of Covid-19 vaccines against the B. 1.617.2 (Delta) variant. *N. Engl. J. Med.* **2021**, *385*, 585−594.

(8) Scudellari, M. How the coronavirus infects cells — and why Delta is so dangerous. *Nature* **2021**, *595*, 640−644.

(9) Singh, J.; Rahman, S. A.; Ehtesham, N. Z.; Hira, S.; Hasnain, S. E. SARS-CoV-2 variants of concern are emerging in India. *Nat. Med.* **2021**, *7*, 1131−1133.

(10) *Risk assessment for SARS-CoV-2 variant Omicron: VOC-21NOV-01 (B1.1.529)*: 22 December 2021; (PDF; 81 KB) UK Health Security Agency (UKHSA), 22 December 2021, p. 1, archived from the original on December 23, 2021; accessed December 23, 2021(English).

(11) Liu, C.; Ginn, H. M.; Dejnirattisai, W.; Supasa, P.; Wang, B.; Tuekprakhon, A.; Nutalai, R.; Zhou, D.; Mentzer, A. J.; Zhao, Y.; Duyvesteyn, H. M. E.; López-Camacho, C.; Slon-Campos, J.; Walter, T. S.; Skelly, D.; Johnson, S. A.; Ritter, T. G.; Mason, C.; Costa Clemens, S. A.; Gomes Naveca, F.; Nascimento, V.; Nascimento, F.; Fernandes da Costa, C.; Resende, P. C.; Pauvolid-Correa, A.; Siqueira, M. M.; Dold, C.; Temperton, N.; Dong, T.; Pollard, A. J.; Knight, J. C.; Crook, D.; Lambe, T.; Clutterbuck, E.; Bibi, S.; Flaxman, A.; Bittaye, M.; Belij-Rammerstorfer, S.; Gilbert, S. C.; Malik, T.; Carroll, M. W.; Klenerman, P.; Barnes, E.; Dunachie, S. J.; Baillie, V.; Serafin, N.; Ditse, Z.; Da Silva, K.; Paterson, N. G.; Williams, M. A.; Hall, D. R.; Madhi, S.; Nunes, M. C.; Goulder, P.; Fry, E. E.; Mongkolsapaya, J.; Ren, J.; Stuart, D. I.; Screaton, G. R. Reduced neutralization of SARS-CoV-2 B.1.617 by vaccine and convalescent serum. *Cell* **2021**, *184*, 4220−4236.

(12) Hoffmann, M.; Krüger, N.; Schulz, S.; Cossmann, A.; Rocha, C.; Kempf, A.; Nehlmeier, I.; Graichen, L.; Moldenhauer, A. S.; Winkler, M. S.; Lier, M.; Dopfer-Jablonka, A.; Jäck, H. M.; Behrens, G. M. N.; Pöhlmann, S. The Omicron variant is highly resistant against antibody-mediated neutralization: Implications for control of the COVID-19 pandemic. *Cell* **2022**, *185*, 447−456.e11.

(13) McCreary, E. K.; Angus, D. C. Efficacy of remdesivir in COVID-19. *JAMA* **2020**, *324*, 1041−1042.

(14) Spinner, C. D.; Gottlieb, R. L.; Criner, G. J.; Arribas López, J. R.; Cattelan, A. M.; Soriano Viladomiu, A.; Ogbuagu, O.; Malhotra, P.; Mullane, K. M.; Castagna, A.; Chai, L. Y. A.; Roestenberg, M.; Tsang, O. T. Y.; Bernasconi, E.; Le Turnier, P.; Chang, S. C.; SenGupta, D.; Hyland, R. H.; Osinusi, A. O.; Cao, H.; Blair, C.; Wang, H.; Gaggar, A.; Brainard, D. M.; McPhail, M. J.; Bhagani, S.; Ahn, M. Y.; Sanyal, A. J.; Huhn, G.; Marty, F. M. GS-US-540-5774 Investigators. Effect of remdesivir vs standard care on clinical status at 11 days in patients with moderate COVID-19: A randomized clinical trial. *JAMA* **2020**, *324*, 1048−1057.

(15) *Coronavirus (COVID-19) Update: FDA Authorizes First Oral Antiviral for Treatment of COVID-19*; FDA, 2021 https://www.fda.gov/news-events/press-announcements/coronavirus-covid-19-update-fda-authorizes-first-oral-antiviral-treatment-covid-19 (updated on December 22, 2021)

(16) Pillaiyar, T.; Meenakshisundaram, S.; Manickam, M. Recent discovery and development of inhibitors targeting coronaviruses. *Drug Discovery Today* **2020**, *25*, 668−688.

(17) Kaul, D. An overview of coronaviruses including the SARS-2 coronavirus - molecular biology, epidemiology and clinical Implication. *Curr. Med. Res. Pract.* **2020**, *10*, 54−64.

(18) Fehr, A.R.; Perlman, S. Coronaviruses: An overview of their replication and pathogenesis. In *Coronaviruses, Methods in Molecular Biology*; Maier, H.; Bickerton, E.; Britton, P. Humana Press: New York, NY, 2015; vol *1282*.

(19) Wan, Y.; Shang, J.; Graham, R.; Baric, R. S.; Li, F. Advances toward curing HIV-1 infection in tissue reservoirs. *J. Virol.* **2020**, *94*, e00127−e00120.

(20) Tse, L. V.; Meganck, R. M.; Graham, R. L.; Baric, R. S. The current and future state of vaccines, antivirals and gene therapies against emerging coronaviruses. *Front. Microbiol.* **2020**, *11*, 495−504.

(21) Chen, Y.; Liu, Q.; Guo, D. Emerging coronaviruses: Genome structure, replication, and pathogenesis. *J. Med. Virol.* **2020**, *92*, 418−423.

(22) Gorbalenya, A. E.; Baker, S. C.; Baric, R. S.; de Groot, R. J.; Drosten, C.; Gulyaeva, A. A.; Haagmans, B. L.; Lauber, C.; Leontovich, A. M.; Neuman, B. W.; Penzar, D.; Perlman, S.; Poon, L. L.; Samborskiy, D. V.; Sidorov, I. A.; Sola, I.; Ziebuhr, J. The species Severe acute respiratory syndrome-related coronavirus: classifying 2019-nCoV and naming it SARS-CoV-2. *Nat. Microbiol.* **2020**, *5*, 536−544.

(23) Pillaiyar, T.; Manickam, M.; Namasivayam, V.; Hayashi, Y.; Jung, S. H. An overview of severe acute respiratory syndrome-coronavirus (SARS-CoV) 3CL protease inhibitors: Peptidomimetics and small molecule chemotherapy. *J. Med. Chem.* **2016**, *59*, 6595−6628.

(24) Pillaiyar, T.; Manickam, M.; Jung, S. H. Middle East respiratory syndrome-coronavirus (MERS-CoV): An updated overview and pharmacotherapeutics. *Med. Chem.* **2015**, *5*, 361−372.

(25) Darling, M. R.; Tsai, S.; Jackson-Boeters, L.; Daley, T. D.; Diamandis, E. P. Human kallikrein 3 (prostate specific antigen) and human kallikrein 5 expression in salivary gland tumors. *Int. J. Biol. Markers* **2006**, *21*, 201−205.

(26) Pillaiyar, T.; Wendt, L. L.; Manickam, M.; Easwaran, M. The recent outbreaks of human coronaviruses: A medicinal chemistry perspective. *Med. Res. Rev.* **2021**, *41*, 72−135.

(27) Cannalire, R.; Cerchia, C.; Beccari, A. R.; Di Leva, F. S.; Summa, V. Targeting SARS-CoV-2 proteases and polymerase for COVID-19 treatment: State of the art and future opportunities. *J. Med. Chem.* **2022**, *65*, 2716−2746.

(28) Gao, K.; Wang, R.; Chen, J.; Tepe, J. J.; Huang, F.; Wei, G. W. Perspectives on SARS-CoV-2 main protease inhibitors. *J. Med. Chem.* **2021**, *64*, 16922−16955.

(29) Bai, B.; Arutyunova, E.; Khan, M. B.; Lu, J.; Joyce, M. A.; Saffran, H.; Shields, J. S.; Kandadai, A. S.; Belovodskiy, A.; Hena, H.; Vuong, W.; Lamer, T.; Young, H.; Vederas, J. C.; Tyrrell, D. L.; Lemieux, M. J.; Nieman, J. Peptidomimetic nitrile warheads as SARS-CoV-2 3CL protease inhibitors. *RSC Med. Chem.* **2021**, *12*, 1722−1730.

(30) Vuong, W.; Fischer, C.; Khan, M. B.; van Belkum, M. J.; Lamer, T.; Willoughby, K. D.; Lu, J.; Arutyunova, E.; Joyce, M. A.; Saffran, H. A.; Shields, J. A.; Young, H. S.; Nieman, J. A.; Tyrrell, L. D.; Lemieux, M. J.; Vederas, J. C. Improved SARS-CoV-2 Mpro inhibitors based on feline antiviral drug GC376: structural enhancements, increased solubility, and micellar studies. *Eur. J. Med. Chem.* **2021**, *222*, 1−11.

(31) Bai, B.; Belovodskiy, A.; Hena, M.; Kandadai, A. S.; Joyce, M. A.; Saffran, H. A.; Shields, J. A.; Khan, M. B.; Arutyunova, E.; Lu, J.; Bajwa, S. K.; Hockman, D.; Fischer, C.; Lamer, T.; Vuong, W.; Van Belkum, M. J.; Gu, Z.; Lin, F.; Du, Y.; Xu, J.; Rahim, M.; Young, H. S.; Vederas, J. C.; Tyrrell, D. L.; Lemieux, M. J.; Nieman, J. Peptidomimetic a-acyloxymethylketone warheads with 6-membered lactam P1 glutamine mimic: SARS-CoV-2 3CL protease inhibition, coronavirus antiviral activity and in vitro biological stability. *J. Med. Chem.* **2022**, *65*, 2905−2925.

(32) Thanigaimalai, P.; Konno, S.; Yamamoto, T.; Koiwai, Y.; Taguchi, A.; Takayama, K.; Yakushiji, F.; Akaji, K.; Chen, S. E.; Naser-Tavakolian, A.; Schön, A.; Freire, E.; Hayashi, Y. Development of potent dipeptide-type SARS-CoV 3CL protease inhibitors with novel P3 scaffolds: design, synthesis, biological evaluation, and docking studies. *Eur. J. Med. Chem.* **2013**, *68*, 372−384.

(33) Thanigaimalai, P.; Konno, S.; Yamamoto, T.; Koiwai, Y.; Taguchi, A.; Takayama, K.; Yakushiji, F.; Akaji, K.; Kawasaki, Y.; Chen, S. E.; Naser-Tavakolian, A.; Schön, A.; Freire, E.; Hayashi, Y. Design, synthesis, and biological evaluation of novel dipeptide-type SARS-CoV 3CL protease inhibitors: structure-activity relationship study. *Eur. J. Med. Chem.* **2013**, *65*, 436−447.

(34) Konno, S.; Thanigaimalai, P.; Yamamoto, T.; Nakada, K.; Kakiuchi, R.; Takayama, K.; Yamazaki, Y.; Yakushiji, F.; Akaji, K.; Kiso, Y.; Kawasaki, Y.; Chen, S. E.; Freire, E.; Hayashi, Y. Design and synthesis of new tripeptide-type SARS-CoV 3CL protease inhibitors containing an electrophilic arylketone moiety. *Bioorg. Med. Chem.* **2013**, *21*, 412−424.

(35) Ghosh, A. K.; Gong, G.; Grum-Tokars, V.; Mulhearn, D. C.; Baker, S. C.; Coughlin, M.; Prabhakar, B. S.; Sleeman, K.; Johnson, M. E.; Mesecar, A. D. Design, synthesis and antiviral efficacy of a series of potent chloropyridyl ester-derived SARS-CoV $3CL^{pro}$ inhibitors. *Bioorg. Med. Chem. Lett.* **2008**, *18*, 5684−5688.

(36) Wu, C. Y.; King, K. Y.; Kuo, C. J.; Fang, J. M.; Wu, Y. T.; Ho, M. Y.; Liao, C. L.; Shie, J. J.; Liang, P. H.; Wong, C. H. Stable benzotriazole esters as mechanism-based inactivators of the severe acute respiratory syndrome 3CL protease. *Chem. Biol.* **2006**, *13*, 261−268.

(37) Breidenbach, J.; Lemke, C.; Pillaiyar, T.; Schäkel, L.; Al Hamwi, G.; Diett, M.; Gedschold, R.; Geiger, N.; Lopez, V.; Mirza, S.; Namasivayam, V.; Schiedel, A. C.; Sylvester, K.; Thimm, D.; Vielmuth, C.; Phuong Vu, L.; Zyulina, M.; Bodem, J.; Gütschow, M.; Müller, C. E. Targeting the main protease of SARS-CoV-2: From the establishment of high throughput screening to the design of tailored inhibitors. *Angew. Chem., Int. Ed.* **2021**, *60*, 10423−10429.

(38) Konno, S.; Kobayashi, K.; Senda, M.; Funai, Y.; Seki, Y.; Tamai, I.; Schäkel, L.; Sakata, K.; Pillaiyar, T.; Taguchi, A.; Taniguchi, A.; Gütschow, M.; Müller, C. E.; Takeuchi, K.; Hirohama, M.; Kawaguchi, A.; Kojima, M.; Senda, T.; Shirasaka, Y.; Kamitani, W.; Hayashi, Y. 3CL Protease inhibitors with an electrophilic arylketone moiety as anti-SARS-CoV-2 agents. *J. Med. Chem.* **2022**, *24*, 2926−2939.

(39) Ghosh, A. K.; Raghavaiah, J.; Shahabi, D.; Yadav, M.; Anson, B. J.; Lendy, E. K.; Hattori, S. I.; Higashi-Kuwata, N.; Mitsuya, H.; Mesecar, A. D. Indole chloropyridinyl ester-derived SARS-CoV-2 $3CL^{pro}$ inhibitors: Enzyme inhibition, antiviral efficacy, structure-activity relationship, and X-ray structural studies. *J. Med. Chem.* **2021**, *64*, 14702−14714.

(40) Ferreira, G. M.; Kronenberger, T.; Tonduru, A. K.; Hirata, R. D. C.; Hirata, M. H.; Poso, A. SARS-COV-2 Mpro conformational changes induced by covalently bound ligands. *J. Biomol. Struct. Dyn.* **2021**, 1−11.

(41) Forster, M.; Chaikuad, A.; Dimitrov, T.; Döring, E.; Holstein, J.; Berger, B. T.; Gehringer, M.; Ghoreschi, K.; Müller, S.; Knapp, S.; Laufer, S. A. Development, optimization, and structure-activity relationships of covalent-reversible JAK3 inhibitors based on a tricyclic imidazo[5,4- d]pyrrolo[2,3- *b*]pyridine scaffold. *J. Med. Chem.* **2018**, *61*, 5350−5366.

(42) Pillaiyar, T.; Laufer, S. Kinases as potential therapeutic targets for anti-coronaviral therapy. *J. Med. Chem.* **2022**, *65*, 955−982.

(43) *Therapeutic Management of Hospitalized Adults With COVID-19*; National Institutes of Health, 2022 https://www.covid19treatmentguidelines.nih.gov/management/clinical-management/hospitalized-adults--therapeutic-management/ (last Updated: December 16, 2021

(44) Viaud, J.; Peterson, J. R. An allosteric kinase inhibitor binds the p21-activated kinase autoregulatory domain covalently. *Mol. Cancer Ther.* **2009**, *8*, 2559−2565.

https://doi.org/10.1021/acs.jmedchem.2c00636
J. Med. Chem. XXXX, XXX, XXX−XXX

(45) Jin, Z.; Du, X.; Xu, Y.; Deng, Y.; Liu, M.; Zhao, Y.; Zhang, B.; Li, X.; Zhang, L.; Peng, C.; Duan, Y.; Yu, J.; Wang, L.; Yang, K.; Liu, F.; Jiang, R.; Yang, X.; You, T.; Liu, X.; Yang, X.; Bai, F.; Liu, H.; Liu, X.; Guddat, L. W.; Xu, W.; Xiao, G.; Qin, C.; Shi, Z.; Jiang, H.; Rao, Z.; Yang, H. Structure of M^{pro} from SARS-CoV-2 and discovery of its inhibitors. *Nature* **2020**, *582*, 289−293.

(46) Sun, W.; Xie, Z.; Liu, Y.; Zhao, D.; Wu, Z.; Zhang, D.; Lv, H.; Tang, S.; Jin, N.; Jiang, H.; Tan, M.; Ding, J.; Luo, C.; Li, J.; Huang, M.; Geng, M. JX06 selectively inhibits pyruvate dehydrogenase kinase PDK1 by a covalent cysteine modification. *Cancer Res.* **2015**, *75*, 4923−4936.

(47) Koch, J.; Uckeley, Z. M.; Doldan, P.; Stanifer, M.; Boulant, S.; Lozach, P. Y. TMPRSS2 expression dictates the entry route used by SARS-CoV-2 to infect host cells. *EMBO J.* **2021**, *40*, No. e107821.

(48) Hoffman, R. L.; Kania, R. S.; Brothers, M. A.; Davies, J. F.; Ferre, R. A.; Gajiwala, K. S.; He, M.; Hogan, R. J.; Kozminski, K.; Li, L. Y.; Lockner, J. W.; Lou, J.; Marra, M. T.; Mitchell, L. J., Jr.; Murray, B. W.; Nieman, J. A.; Noell, S.; Planken, S. P.; Rowe, T.; Ryan, K.; Smith, G. J. I. I. I.; Solowiej, J. E.; Steppan, C. M.; Taggart, B. Discovery of ketone-based covalent inhibitors of coronavirus 3CL proteases for the potential therapeutic treatment of COVID-19. *J. Med. Chem.* **2020**, *63*, 12725−12747.

(49) de Vries, M.; Mohamed, A. S.; Prescott, R. A.; Valero-Jimenez, A. M.; Desvignes, L.; O'Connor, R.; Steppan, C.; Devlin, J. C.; Ivanova, E.; Herrera, A.; Schinlever, A.; Loose, P.; Ruggles, K.; Koralov, S. B.; Anderson, A. S.; Binder, J. Dittmann. M. A comparative analysis of SARS-CoV-2 antivirals characterizes $3CL^{pro}$ inhibitor PF-00835231 as a potential new treatment for COVID-19. *J. Virol.* **2021**, *95*, e01819−e01820.

(50) He, X.; Quan, S.; Xu, M.; Rodriguez, S.; Goh, S. L.; Wei, J.; Fridman, A.; Koeplinger, K. A.; Carroll, S. S.; Grobler, J. A.; Espeseth, A. S.; Olsen, D. B.; Hazuda, D. J.; Wang, D. Generation of SARS-CoV-2 reporter replicon for high-throughput antiviral screening and testing. *PNAS* **2021**, *118*, No. e2025866118.

(51) Tomar, S.; Johnston, M. L.; St John, S. E.; Osswald, H. L.; Nyalapatla, P. R.; Paul, L. N.; Ghosh, A. K.; Denison, M. R.; Mesecar, A. D. Ligand-induced dimerization of Middle East respiratory syndrome (MERS) coronavirus nsp5 protease ($3CL^{pro}$): Implications for nsp5 regulation and the development of antivirals. *J. Biol. Chem.* **2015**, *290*, 19403−19422.

(52) Wu, A.; Wang, Y.; Zeng, C.; Huang, X.; Xu, S.; Su, C.; Wang, M.; Chen, Y.; Guo, D. Prediction and biochemical analysis of putative cleavage sites of the 3C-like protease of Middle East respiratory syndrome coronavirus. *Virus Res.* **2015**, *208*, 56−65.

(53) Chen, Y. W.; Yiu, C. P. B.; Wong, K. Y. Prediction of the SARS-CoV-2 (2019-nCoV) 3C-like protease ($3CL^{pro}$) structure: Virtual screening reveals velpatasvir, ledipasvir, and other drug repurposing candidates. *F1000Research* **2020**, *9*, 129.

(54) Vuong, W.; Khan, M. B.; Fischer, C.; Arutyunova, E.; Lamer, T.; Shields, J.; Saffran, H. A.; McKay, R. T.; van Belkum, M. J.; Joyce, M. A.; Young, H. S.; Tyrrell, D. L.; Vederas, J. C.; Lemieux, M. J. Feline coronavirus drug inhibits the main protease of SARS-CoV-2 and blocks virus replication. *Nat. Commun.* **2020**, *11*, 5409.

(55) Bzówka, M.; Mitusińska, K.; Raczyńska, A.; Samol, A.; Tuszyński, J. A.; Góra, A. Structural and evolutionary analysis indicate that the SARS-CoV-2 M^{pro} is a challenging target for small-molecule inhibitor design. *Int. J. Mol. Sci.* **2020**, *21*, 3099.

(56) Douangamath, A.; Fearon, D.; Gehrtz, P.; Krojer, T.; Lukacik, P.; Owen, C. D.; Resnick, E.; Strain-Damerell, C.; Aimon, A.; Ábrányi-Balogh, P.; Brandão-Neto, J.; Carbery, A.; Davison, G.; Dias, A.; Downes, T. D.; Dunnett, L.; Fairhead, M.; Firth, J. D.; Jones, S. P.; Keeley, A.; Keserü, G. M.; Klein, H. F.; Martin, M. P.; Noble, M. E. M.; O'Brien, P.; Powell, A.; Reddi, R. N.; Skyner, R.; Snee, M.; Waring, M. J.; Wild, C.; London, N.; von Delft, F.; Walsh, M. A. Crystallographic and electrophilic fragment screening of the SARS-CoV-2 main protease. *Nat. Commun.* **2020**, *11*, 5047.

(57) Halgren, T. A.; Murphy, R. B.; Friesner, R. A.; Beard, H. S.; Frye, L. L.; Pollard, W. T.; Banks, J. L. Glide: a new approach for rapid, accurate docking and scoring. 2. Enrichment factors in database screening. *J. Med. Chem.* **2004**, *47*, 1750−1759.

(58) Zhu, K.; Borrelli, K. W.; Greenwood, J. R.; Day, T.; Abel, R.; Farid, R. S.; Harder, E. Docking covalent inhibitors: a parameter free approach to pose prediction and scoring. *J. Chem. Inf. Model.* **2014**, *54*, 1932−1940.

(59) Jacobson, M. P.; Pincus, D. L.; Rapp, C. S.; Day, T. J.; Honig, B.; Shaw, D. E.; Friesner, R. A. A hierarchical approach to all-atom protein loop prediction *Proteins: Struct. Funct. Genet.* **2004**, *55*, 351−367.

(60) Jacobson, M. P.; Friesner, R. A.; Xiang, Z.; Honig, B. On the role of the crystal environment in determining protein side-chain conformations. *Mol. Biol.* **2002**, *320*, 597−608.

(61) Bowers, K.J.; Chow, H. E.; Xu, R.O.; Dror, M.P.; Eastwood, B.A.; Gregersen, J.L.; Klepeis, I.; Kolossvary, M.A.; Moraes, F.D.; Sacerdoti, J.K.; Salmon, Y.; Shan, D.E. *Proceedings of the 2006 ACM/IEEE Conference on Supercomputing*; SC '06; ACM: New York, NY, USA, 2006. DOI: 10.1145/1188455.1188544.

(62) Lu, C.; Wu, C.; Ghoreishi, D.; Chen, W.; Wang, L.; Damm, W.; Ross, G. A.; Dahlgren, M. K.; Russell, E.; Von Bargen, C. D.; Abel, R.; Friesner, R. A.; Harder, E. D. OPLS4: Improving force field accuracy on challenging regimes of chemical space. *J. Chem. Theory Comput.* **2021**, *17*, 4291−4300.

(63) Jorgensen, W. L.; Chandrasekhar, J.; Madura, J. D.; Impey, R. W.; Klein, M. L. Comparison of simple potential functions for simulating liquid water. *J. Chem. Phys.* **1983**, *79*, 926−935.

(64) Darden, T.; York, D.; Pedersen, L. Particle mesh Ewald: An N·log(N) method for Ewald sums in large systems. *J. Chem. Phys.* **1993**, *98*, 10089−10092.

(65) Chen, Y. W.; Yiu, C. B.; Wong, K. Y. Prediction of the SARS-CoV-2 (2019-nCoV) 3C-like protease (3CL pro) structure: Virtual screening reveals velpatasvir, ledipasvir, and other drug repurposing candidates. *F1000Research* **2020**, *9*, 129.

(66) *GraphPad Prism*, version 6.00, La Jolla, California, USA

(67) Su, H. X.; Yao, S.; Zhao, W. F.; Li, M. J.; Liu, J.; Shang, W. J.; Xie, H.; Ke, C. Q.; Hu, H. C.; Gao, M. N.; Yu, K. Q.; Liu, H.; Shen, J. S.; Tang, W.; Zhang, L. K.; Xiao, G. F.; Ni, L.; Wang, D. W.; Zuo, J. P.; Jiang, H. L.; Bai, F.; Wu, Y.; Ye, Y.; Xu, Y. C. Anti-SARS-CoV-2 activities in vitro of Shuanghuanglian preparations and bioactive ingredients. *Acta Pharmacol. Sin.* **2020**, *41*, 1167−1177.

(68) Emsley, P.; Cowtan, K. Coot: Model-building tools for molecular graphics. *Acta Crystallogr., D* **2004**, *60*, 2126−2132.

(69) Adams, P. D.; Grosse-Kunstleve, R. W.; Hung, L. W.; Ioerger, T. R.; McCoy, A. J.; Moriarty, N. W.; Read, R. J.; Sacchettini, J. C.; Sauter, N. K.; Terwilliger, T. C. PHENIX: building new software for automated crystallographic structure determination. *Acta Crystallogr., D* **2002**, *58*, 1948−1954.

(70) Keeley, A.; Ábrányi-Balogh, P.; Keserű, G. M. Design and characterization of a heterocyclic electrophilic fragment library for the discovery of cysteine-targeted covalent inhibitors. *MedChemCommun.* **2019**, *10*, 263−267.

(71) Forster, M.; Liang, X. J.; Schröder, M.; Gerstenecker, S.; Chaikuad, A.; Knapp, S.; Laufer, S.; Gehringer, M. Discovery of a novel class of covalent dual inhibitors targeting the protein kinases BMX and BTK. *Int. J. Mol. Sci.* **2020**, *21*, 9269.